

# Dynamic history of the inner core constrained by seismic anisotropy

Daniel Frost (✉ [dafrost@berkeley.edu](mailto:dafrost@berkeley.edu))

University of California Berkeley

Marine Lasbleis

Université de Nantes

Brian Chandler

University of California, Berkeley

Barbara Romanowicz

University of California <https://orcid.org/0000-0002-6208-6044>

---

## Article

**Keywords:** Progressive crystallization, Convection, Magnetic Field, Geodynamo, Deformation Texturing, Solid-fluid Boundary, Mineral Physics

**Posted Date:** January 5th, 2021

**DOI:** <https://doi.org/10.21203/rs.3.rs-87174/v1>

**License:**   This work is licensed under a Creative Commons Attribution 4.0 International License.

[Read Full License](#)

---

**Version of Record:** A version of this preprint was published at Nature Geoscience on June 3rd, 2021. See the published version at <https://doi.org/10.1038/s41561-021-00761-w>.

1 **Title:** Dynamic history of the inner core constrained by seismic anisotropy

2  
3 **Authors:** Daniel A. Frost<sup>1\*</sup>, Marine Lasbleis<sup>2,3</sup>, Brian Chandler<sup>1</sup>, Barbara Romanowicz<sup>1,4,5</sup>

4  
5 **Affiliations:**

6 <sup>1</sup>Department of Earth & Planetary Science, University of California, Berkeley, CA, USA.

7 <sup>2</sup> Laboratoire de Planétologie et Géodynamique, UMR 6112, Université de Nantes, CNRS,  
8 France

9 <sup>3</sup>Earth-Life Science Institute, Tokyo Institute of Technology, Meguro, Tokyo 152-8551, Japan

10 <sup>4</sup> Collège de France, Paris, France.

11 <sup>5</sup> Université de Paris, Institut de Physique du Globe de Paris, Paris, France.

12  
13 \*Correspondence to: dafrost@berkeley.edu

14  
15 **Progressive crystallisation of Earth's inner core over geological times drives**  
16 **convection in the outer core and the generation of the Earth's magnetic field.**  
17 **Resolving the rate and pattern of inner core growth is thus crucial to understanding**  
18 **the evolution of the geodynamo. The growth history of Earth's inner core is likely**  
19 **recorded in the distribution and strength of seismic anisotropy arising from**  
20 **deformation texturing constrained by boundary conditions at the inner-core solid-**  
21 **fluid boundary. Travel times of seismic body waves indicate that seismic anisotropy**  
22 **increases with depth. Here we find that the strongest anisotropy is offset from Earth's**  
23 **rotation axis. Using geodynamic growth models and mineral physics calculations, we**  
24 **simulate the development of inner core anisotropy in a self-consistent manner. We**  
25 **show for the first time that an inner core model composed of hexagonally close-**  
26 **packed iron-nickel alloy, deformed by a combination of preferential equatorial**  
27 **growth and slow translation can match the seismic observations without requiring the**  
28 **introduction of hemispheres with sharp boundaries. We find a model of the inner core**  
29 **growth history compatible with external constraints from outer core dynamics,**  
30 **supporting arguments for a relatively young inner core (~0.5-1.5 Ga) and a viscosity**  
31 **>10<sup>18</sup> Pa-s.**

32  
33 The presence of seismic anisotropy - the dependence of seismic wavespeed on direction of  
34 propagation - in the inner core (IC) was proposed over 30 years ago to explain the early  
35 arrival times of IC sensitive seismic body waves (PKP<sub>df</sub>) travelling on paths parallel to the  
36 Earth's rotation axis<sup>1,2</sup> and anomalous splitting of core-sensitive free oscillations<sup>3</sup>. This  
37 anisotropy is thought to result from alignment of iron crystals caused by deformation in a  
38 flow field induced by the evolution of the core, i.e. deformation texturing. In previous work,  
39 different geodynamic<sup>4</sup> and plastic deformation mechanisms<sup>5</sup> were explored to explain the  
40 variation of PKP<sub>df</sub> travel times with angle of the ray path with respect to the rotation axis.  
41 Here, for the first time, we combine geodynamic modelling of the evolution of flow in the IC,  
42 allowing for slow lateral translation, with presently available knowledge on the mineralogy  
43 and deformation mechanisms proposed for the IC to explain spatially varying patterns of  
44 observed seismic travel times in an updated global dataset.

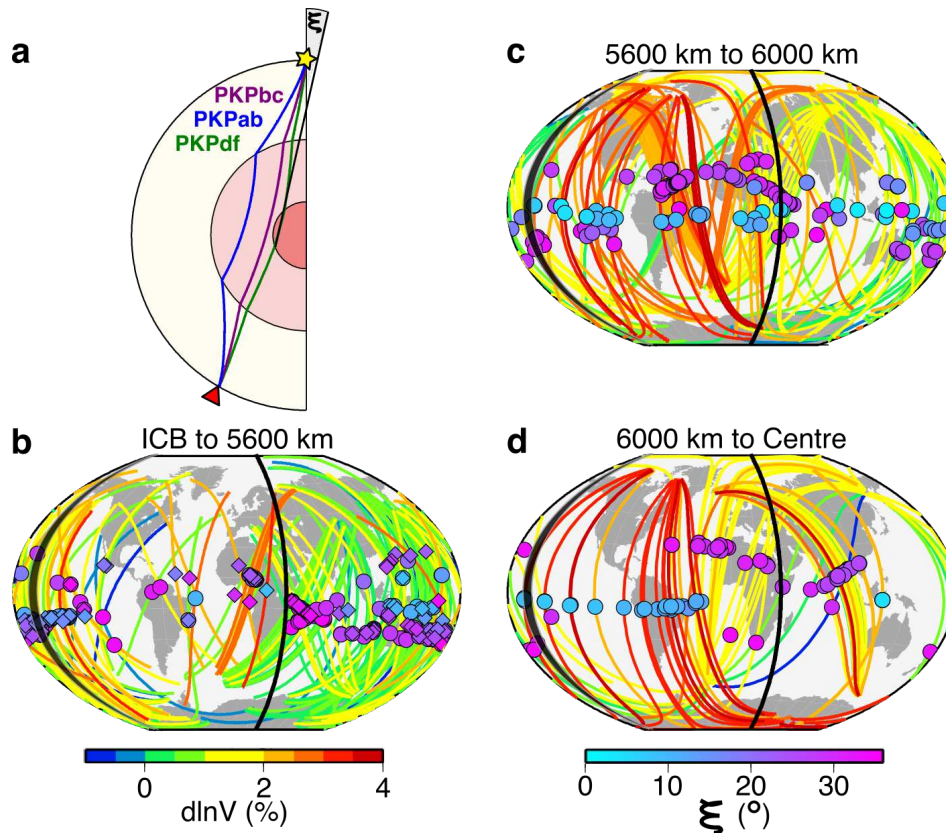
45

46 Indeed, in early models of seismic anisotropy based on measurements of PKP<sub>df</sub> travel times,  
47 constant cylindrical anisotropy was considered, with the fast axis parallel to Earth's rotation  
48 axis. Since then, further work on IC structure has revealed increasing complexity. Recent IC  
49 models comprise two quasi-hemispheres of differing strengths of anisotropy, ~4.8% on  
50 average in the quasi-western hemisphere (WH), and ~1.4% in the quasi-eastern hemisphere  
51 (EH)<sup>6-8</sup>. An increase of anisotropy strength with depth in the IC has also been documented,  
52 with some studies suggesting values reaching up to 8.8% at the centre of the IC<sup>9</sup>. However,  
53 these models suffer from the poor data coverage on polar paths, due to the limited global  
54 distribution of earthquakes and stations.

55  
56 In an effort to address this issue, we have made new differential travel time measurements  
57 of PKP<sub>ab-df</sub> and PKP<sub>bc-df</sub> from recent seismic deployments (Fig. 1 and Extended Data Fig.  
58 1) that increase sampling of the IC along polar directions at a large range of depths and added  
59 them to our existing global collection (See Methods). The updated dataset samples the IC  
60 close to Earth's rotation axis: from the inner core boundary (ICB) to within 35 km of the  
61 centre of the Earth.

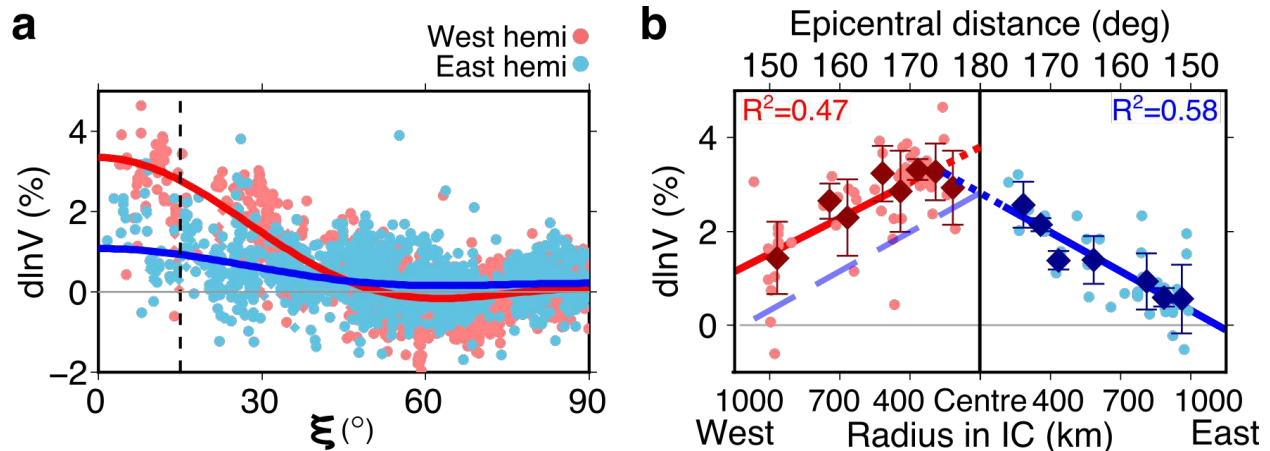
62  
63 Differential travel time anomalies, expressed as the effective velocity anomaly within the  
64 inner core ( $d\ln V = -\frac{dT}{T_{ic}}$ , where  $T_{ic}$  is the travel time through the IC) exhibit a strong  
65 dependence on  $\xi$ , the angle of the path within the IC with respect to the rotation axis (Fig.  
66 1a), with residuals of up to 9.9 s at the largest distances for polar paths, and  $\pm 2$  s for more  
67 equatorial paths (Extended Data Fig. 2). Furthermore, the residuals show clear dependence  
68 on both the longitude and depth of the turning point of the ray (Fig. 1b,c,d). To first order, as  
69 found previously<sup>6-9</sup>, the data exhibit hemispherical differences (Fig. 1 and Extended Data Fig.  
70 4). Assuming a linear dependence of anisotropy on depth in each hemisphere, we determine  
71 the best fitting western boundary of the WH to be between -166°E and -154°E, but most  
72 likely between -166°E and -159°E (Methods and Extended Data Fig. 5). However, sharp  
73 hemispherical boundaries are difficult to reconcile with geodynamic models of IC growth.

74



75

76 **Fig. 1: Sampling of the inner core with polar PKP rays.** (a) Ray paths of PKP branches  
 77 used in this study. PKPdf samples the inner core, while PKPbc and PKPab remain in the outer  
 78 core.  $\xi$  is the angle that the PKPdf path in the IC makes with Earth's rotation axis. (b-d): Polar  
 79 paths ( $\xi < 35^\circ$ ) from source to receiver colour-coded by effective velocity anomaly in the IC  
 80 (line colour) and  $\xi$  (symbol colour) for paths turning between (b) 5200 and 5600 km depth,  
 81 (c) 5600 km and 6000 km, and (d) 6000 km and Earth's centre. The total number of polar  
 82 paths displayed is 530. The location of turning points for PKPdf rays are shown as diamonds  
 83 (for PKPbc-df) and circles (for PKPab-df). Data shown exclude the South Sandwich Islands  
 84 (SSI) to Alaska paths (see Methods and Extended Data Fig. 3). Equatorial paths are not  
 85 displayed. Grey region marks best-fitting WH boundaries determined in this study (see  
 86 Methods) and solid line marks the EH boundary<sup>10</sup>.  
 87

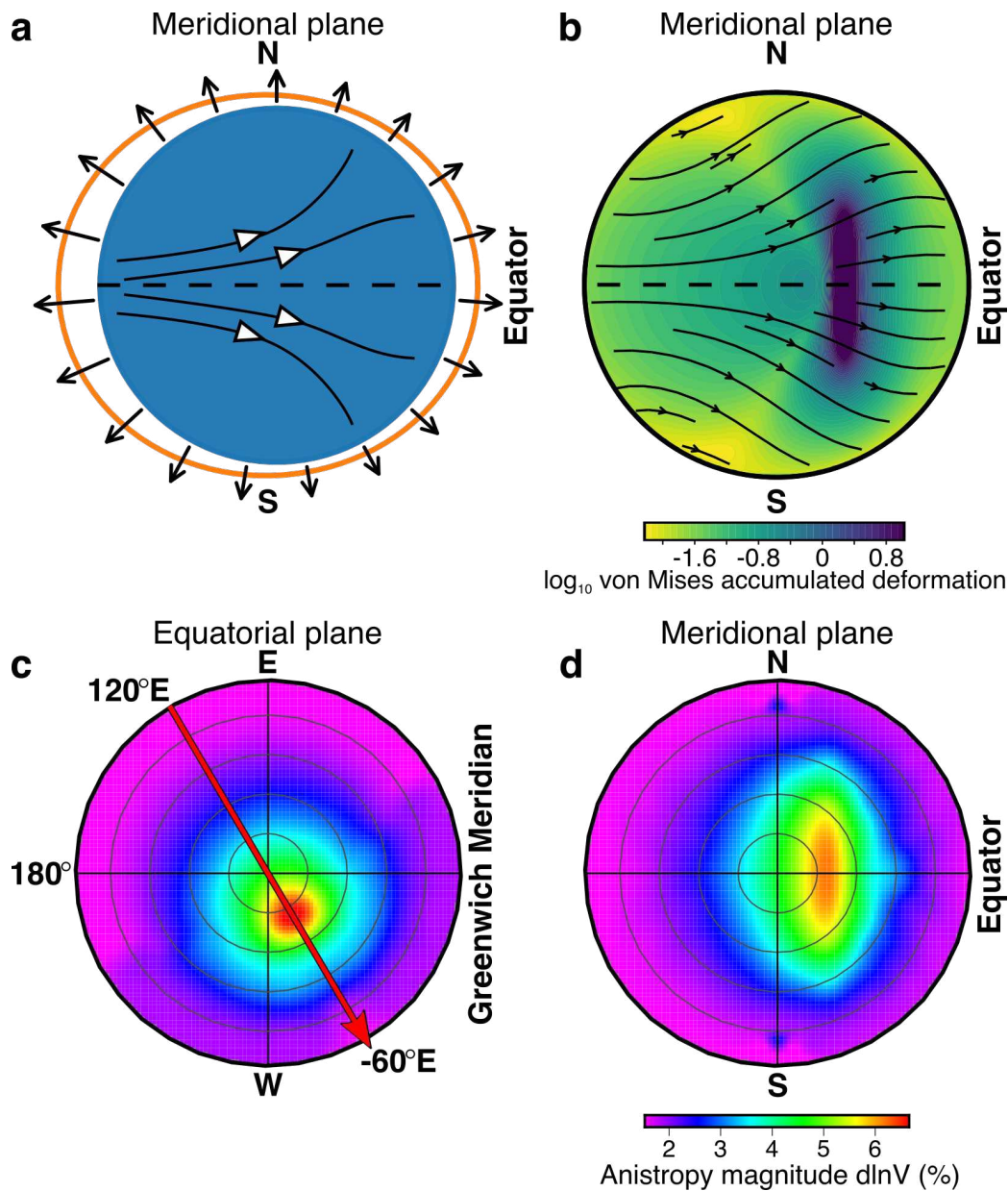


88  
 89 **Fig. 2: Effective velocity anomaly in the inner core from travel time observations as a**  
 90 **function of  $\xi$  and epicentral distance. (a)** Differential PKPab-df and PKPbc-df travel time  
 91 anomalies as a function of  $\xi$ , expressed as effective velocity anomaly in the inner core, display  
 92 a hemispherically distinct pattern implying stronger anisotropy in the WH (red) than in the  
 93 EH (blue). Data from sources in the SSI to stations in Alaska are excluded (See Methods). **(b)**  
 94 Effective IC velocity anomaly as a function of epicentral distance, and thus bottoming radius  
 95 of the ray in the WH (left) and EH (right), for data with  $\xi \leq 15^\circ$  (those data that are left of the  
 96 vertical broken line in (a)). Solid coloured lines indicate linear fits as a function of distance in  
 97 the respective hemispheres with a mirror image across the centre of the Earth ( $180^\circ$ ) for the  
 98 EH shown as a broken line. Moving averages (diamonds) and standard deviations at  $2.5^\circ$   
 99 increments in distance highlight the robustness of these trends. The extension of EH trend  
 100 to meet the WH trend at  $\sim 175^\circ$  distance and 400 km radius is shown as a dotted blue line.

101  
 102 Examining the data more closely, we find that the effective velocity anomaly linearly  
 103 increases with distance, i.e. turning point radius in the IC, in both hemispheres (Fig. 2b). The  
 104 gradient with distance is approximately equal in both hemispheres, but with an offset to  
 105 larger anomalies in the WH. This gradient is dependent on  $\xi$  and is steepest and most  
 106 robustly defined for polar paths ( $0 < \xi < 15^\circ$ ) (Extended Data Fig. 6). The largest effective  
 107 velocity anomalies are recorded in the WH, for rays bottoming at around 400 km radius with  
 108 longitude  $\sim 60^\circ W$  ( $\geq 3.5\%$   $dlnV$  at distances  $\geq 170^\circ$  in the WH, Fig. 2b), not at the centre of the  
 109 IC. Our travel time data thus suggest a depth-dependence of anisotropy that, to first order, is  
 110 smooth and asymmetric with respect to the centre of the Earth, rather than a hemispherical  
 111 pattern with sharp boundaries between the hemispheres.

112  
 113 In order to interpret the seismological observations, we consider the fact that the core likely  
 114 grows preferentially at the equator due to Taylor column convection in the outer core, which  
 115 induces more efficient heat transport in the cylindrically radial direction<sup>11,12</sup>. Isostatic  
 116 adjustment would cause the oblate inner core to flow inwards from the equator and up  
 117 towards the poles<sup>11,13</sup>. Such a flow would be confined to the uppermost layer if a strong  
 118 density stratification existed, and would induce deformation at depth if not<sup>13</sup>. Any  
 119 asymmetry to the heat extraction from the IC in the plane of the equator would cause  
 120 asymmetric growth<sup>12,14</sup> resulting in lateral advection of the growing IC and thus slow net  
 121 translation. Previous studies attempted to explain the depth dependence of anisotropy by  
 122 degree 2 flow<sup>11,14</sup> on the one hand, and the hemispherical dichotomy by degree 1 flow<sup>15,16</sup> on

123 the other. However, these hemispherical studies considered fast convective instabilities  
124 resulting in a degree 1 flow that, alone, could not produce the observed seismic anisotropy  
125 pattern and strength. Guided by our seismic observations, we combine the processes of  
126 preferred equatorial growth and hemispherically asymmetric growth and then analytically  
127 model the flow pattern in a neutrally stratified IC (Fig. 3; see Methods). Advection of strained  
128 crystals along the translation axis shifts the pattern of high deformation laterally from the  
129 axis of rotation, where the amount of lateral offset between the high deformation zone and  
130 the rotation axis depends on the translation rate chosen. A key assumption in our study is  
131 that the translation rate is slow, slower than the rate of growth, as it results from differential  
132 growth<sup>14</sup>, and not from simultaneous melting and freezing on opposite hemispheres<sup>15,16</sup>.  
133 Given the limited constraints, the age of the IC and the translation velocity are both free  
134 parameters of such a model. The differential growth rate of the IC between the equator and  
135 the poles is described by the parameter  $S_2$ , which controls the magnitude and pattern of  
136 strain experienced.  $S_2$  is loosely constrained to be in the range  $0 < S_2 < 1$  from dynamical  
137 arguments<sup>11</sup>, while geodynamical models of the outer core<sup>12,14</sup> argue for a value of  $\sim 0.4$ .  
138 Constraints on  $S_2$  are not very strong, however additional information can be brought in  
139 from mineral physics, which provides constraints on strain rate dependent development of  
140 anisotropy.



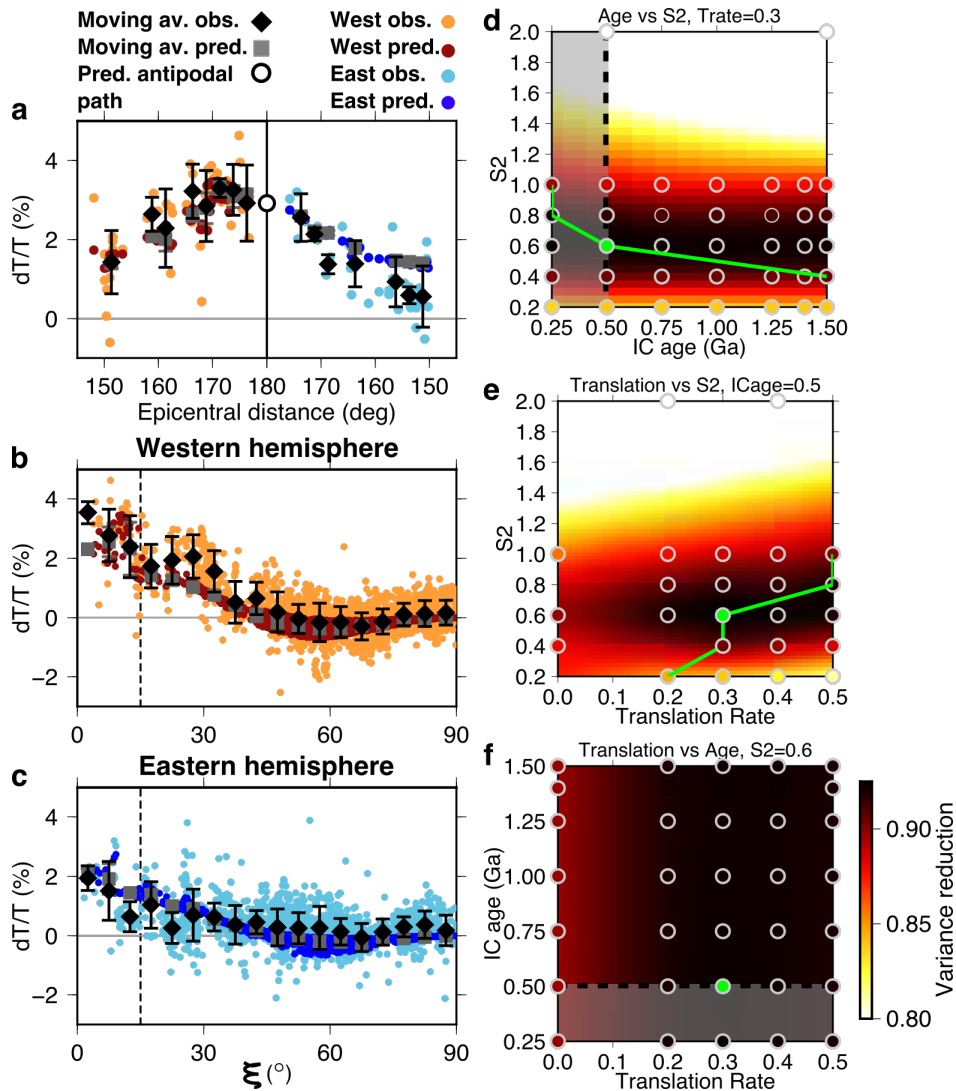
141  
 142 **Fig. 3: Inner core growth, strain and anisotropy.** (a) Sketch combining preferential  
 143 equatorial growth (driven by Taylor column convection in the outer core) and asymmetric  
 144 growth rate, with imposed inner core growth rate at the boundary and internal flow shown  
 145 by black and white arrows, respectively. (b) Asymmetric growth and movement in from the  
 146 equator and towards the poles lead to lateral and vertical advection of the strongest  
 147 deformation. Both (a) and (b) are drawn in the meridional plane along the axis of translation  
 148 with dashed line showing the equator. The strain field aligns hcp iron grains, producing  
 149 strong anisotropy in the deep IC that is offset from the rotation (N-S) axis, as shown in (c)  
 150 in the equatorial plane, and elongated parallel to the rotation axis, as shown in (d) the  
 151 meridional plane along the direction of translation is shown by the red arrow in (c).  
 152 Calculated with IC age of 0.5 Ga, S2 of 0.6, translation rate of 0.3, and translation direction  
 153 from 120°E to -60°W.

154

155 In our model, the present-day IC seismic anisotropy is a function of the initial single crystal  
156 anisotropy, the slip planes of crystal deformation, and the flow field. Crystallographic  
157 alignment of a polycrystal is necessary to generate significant anisotropy on the length scale  
158 of the inner core. Using Visco-Plastic Self-Consistent modelling (VPSC)<sup>17</sup> we calculate the  
159 anisotropy that results from dislocation creep in the strain field produced by our geodynamic  
160 models, for different assumptions on age of the IC and translation rates. Dislocation creep  
161 implies a non-linear relation between stress and strain rate (see Methods), implying that the  
162 degree and pattern of crystal alignment - and therefore the pattern and strength of the  
163 resulting seismic anisotropy varies with duration, and so inner core age. We test different  
164 single crystal structures. Despite body-centred cubic (bcc) iron having strong single crystal  
165 anisotropy<sup>18</sup>, we find that it cannot produce strong polycrystal anisotropy, nor can face-  
166 centered cubic iron, as also previously shown<sup>19</sup>. In contrast, plastic deformation of a  
167 hexagonally close packed (hcp) iron-nickel alloy (Fe<sub>93.75</sub>Ni<sub>6.25</sub>)<sup>20</sup>, compatible with cosmo-  
168 chemical constraints<sup>21</sup>, with slip on the <c+a> pyramidal planes<sup>22,23</sup> produces an anisotropic  
169 inner core with up to 6.6% anisotropy (Fig. 3d) that can fit the seismic data well. In this  
170 model, the fast direction of anisotropy becomes aligned with the rotation axis and the slow  
171 direction varies with depth (Extended Data Fig. 7), matching observations<sup>24</sup>. Pure hcp iron  
172 does not produce as strong a match to our observations (Extended Data Figs. 8 and 9).

173  
174 The pattern and strength of the flow field induced by inner core growth impacts the strain  
175 that crystals experience, and is controlled by the IC age, S2, translation rate, and the direction  
176 of translation. The IC age trades off linearly with strain rate and duration, but the final  
177 seismic anisotropy depends non-linearly on the age through the effect of non-linear  
178 dislocation creep. The total strain is controlled by the parameter S2; thus, the strain rate is  
179 controlled by both IC age and S2. We constrain the inner core growth history by running  
180 models with a range of ages, translation rates, and values of S2 and compare predicted  
181 anisotropy from these models with our seismic observations (Figure 4). The data is best fit  
182 by models with  $0.4 \leq S2 \leq 0.8$ . Within the range of acceptable IC ages<sup>23-25</sup> (see Methods), we  
183 find S2=0.6 and IC age of 0.5 Ga to best fit both the seismic observations and geodynamic  
184 constraints, although the constraint on age is not strong (Fig. 4d-f; See Methods). Translation  
185 at a rate of 0.3 IC radii over the 0.5 Ga IC lifetime along an axis oriented in the equatorial  
186 plane from 120°E towards -60°W matches the geographic pattern of anisotropy, achieving a  
187 93% variance reduction for the polar data compared with 89% for a model with no  
188 translation. Our model shows increasing anisotropy strength with depth. The model also  
189 displays weak anisotropy near the ICB that is stronger in the WH than the EH, which is  
190 qualitatively compatible with models of hemispherically distinct isotropy in the upper inner  
191 core from measurements of PKiKP<sup>25</sup> and P'P'df<sup>26</sup> travel times, and with constraints on the  
192 magnitude and distribution of anisotropy from normal modes<sup>27,28</sup>.

193



194  
 195 **Fig. 4: Predicted versus observed PKP velocity anomalies for hcp Fe<sub>93.75</sub>Ni<sub>6.25</sub> at**  
 196 **5500 K and 360 GPa<sup>20</sup> and trade-offs between IC age, S<sub>2</sub>, and translation rate. (a-c):**  
 197 Predicted (dark blue and red dots and with mean as grey squares) and observed (light blue  
 198 and orange dots and with mean as black diamonds) effective velocity anomalies as a function  
 199 of (a) epicentral distance for data with  $\xi \leq 15^\circ$ , marked by dashed line in (b) and (c), and as a  
 200 function of  $\xi$  in the (b) western and (c) eastern hemispheres for an IC growth model with IC  
 201 age=0.5 Ga, S<sub>2</sub>=0.6, translation rate=0.3, and translation direction from 120°E to -60°W. The  
 202 open circle in (a) marks the predicted effective velocity anomaly for a path along the rotation  
 203 axis. Error bars for the data show the mean and one standard deviation at 2.5° and 5°  
 204 increments for panels (a), and (b) and (c), respectively. For calculation using pure hcp Fe  
 205 see Extended Data Fig. 8. (d-f): Variance reduction of the model relative to the data  
 206 illustrating the trade-offs between (d) IC age and S<sub>2</sub>, (e) S<sub>2</sub> and translation rate, and (f)  
 207 translation rate and IC age. Grey circles mark tested values and the green point marks the  
 208 best-fitting parameters, corresponding to the model in (a-c) and at which the 3D space is  
 209 sampled. The green line tracks the best x-value at any given y-value. Models in the shaded  
 210 region have IC ages that are likely too low based on core conductivity. Surface is interpolated  
 211 with a “minimum curvature” spline.

212  
213 Remaining discrepancies between observations and predictions may result from  
214 contamination of the observations by mantle structure and small-scale structure in the inner  
215 core. While differential measurements help remove the effect of upper mantle heterogeneity  
216 on the PKP travel times to some degree, even modest 3D velocity structure deeper in the  
217 mantle can influence them<sup>29</sup>. The largest travel time anomalies that we observe (<9.9 s) are  
218 for PKPab-df measurements between 170° and 175° distance, where there is large lateral  
219 separation between the two ray paths in the deep mantle, such that they could experience  
220 significantly different mantle velocity structure. Still, mantle velocity anomalies such as Ultra  
221 Low Velocity Zones (ULVZ) and the Large Low Shear Velocity Provinces (LLSVPs) could  
222 generate at most 1-2s travel time delays. Furthermore, the data with large travel time  
223 anomalies pierce the core-mantle boundary at distinctly different locations (Fig. 1b,c,d), and  
224 no ULVZs have yet been reported in these regions<sup>30</sup>. Thus, mantle structure would mostly  
225 introduce scatter and not significantly obscure the first-order inner core anisotropic pattern  
226 that we are able to model.

227  
228 Within the limits of the assumptions made, and in particular the assumption of dislocation  
229 creep, the proposed model has implications for the physical properties of the IC. The  
230 assumption of Yoshida-style deformation restricts the range of possible viscosities for the IC  
231 ( $\eta > 10^{18}$  Pas), and an IC age larger than the diffusive time scale, which may range from 0.2  
232 to 1.5 Ga<sup>4</sup>, depending on the chosen core conductivity. This constraint places the viscosity at  
233 the upper end of the range recently obtained by density function theory<sup>31</sup>.

234  
235 Our model suggests that the seismic structure of the inner core records the large-scale  
236 pattern of the heat flux at the ICB, which is controlled by the dynamics of the outer core and  
237 the heat flux variations at the CMB<sup>12</sup>. Our preferred model has a translation rate of 0.3 and a  
238 ratio of polar to equatorial growth (S2) of 0.6. This causes regional variation of the IC growth  
239 rate measured relative to the global average growth rate. Our model corresponds to a growth  
240 rate at the poles that is 40% lower at the poles and 130% larger at the equator compared to  
241 the global average, and a variation in growth rate between the eastern and western  
242 hemispheres at the equator from 100% to 160% of the global average rate, respectively. This  
243 pattern is similar to that obtained when forcing the geodynamo with heat fluxes at the top of  
244 the core based on the current structure of the lower mantle<sup>12</sup> and suggests that the  
245 asymmetry in heat extraction has been stable in the outer core for times similar to the age of  
246 the inner core. This is in line with indications that the currently observed large low shear  
247 velocity provinces (LLSVP) separated by a ring of high seismic velocities at the base of the  
248 mantle may have been stable for at least 200-300 Ma<sup>32-34</sup>, and with the potential existence  
249 of structures in the mantle stabilizing the convection pattern<sup>35</sup>. In contrast, geomagnetic  
250 observations of outer core patterns that imply forcing by bottom-up interactions<sup>36</sup> may  
251 indicate either a recent change in inner core dynamics from passive to active dynamics or  
252 complex interactions between the inner and outer core that may be described at smaller  
253 scales than are considered here. Our modeling supports a relatively high core conductivity,  
254 as it favors a young inner core age (~0.5 Ga) and requires the absence of convective  
255 instabilities. To prevent the development of thermal instabilities with an inner core age of  
256 0.5 Ga, the thermal conductivity of the inner core has to be larger than 120 W/m/K<sup>4</sup>.  
257 Improved resolution of the 3D patterns of seismic anisotropy in the inner core may help

258 document further the uneven growth history of the inner core, providing a record of the  
259 global scale pattern of outer core dynamics. While our model does not consider the smaller-  
260 scale seismic structure of the inner core<sup>37</sup>, we provide the first holistic model of IC growth  
261 capable of matching the observed seismic anisotropy and consistent with available  
262 paleomagnetic observations and mineral physics data<sup>38,39</sup>.

263 **Methods for:** Seismic evidence of slow translation and preferential equatorial growth of the  
264 inner core

265  
266 **Authors:** Daniel A. Frost<sup>1\*</sup>, Barbara Romanowicz<sup>123</sup>, Marine Lasbleis<sup>45</sup>, Brian Chandler<sup>1</sup>

267  
268  
269 **Seismology**  
270 We collect PKPab-df and PKPbc-df differential travel time measurements to determine inner  
271 core structure (Fig. 1). Differential travel time anomalies, calculated with respect to a 1D  
272 reference model, can thus be attributed to the IC, at least to first order.

273  
274 Our dataset comprises the existing Berkeley (UCB) PKP travel time data collection<sup>24,40-42</sup>  
275 with additional data<sup>43</sup>. This collection includes 2944 and 1170 PKPab-df and PKPbc-df  
276 differential travel time measurements, respectively. Here, we have added a total of 614  
277 PKPab-df and 416 PKPbc-df measurements from both recent events in the South Sandwich  
278 Islands between 23/10/2015 and 15/09/2017 observed in Alaska and other nearby stations  
279 in the northern hemisphere, and from events of  $m > 5.5$  at latitudes greater than  $50^\circ\text{N}$   
280 between 1/1/2008 and 31/06/2017 observed at distances beyond  $150^\circ$  and stations in the  
281 southern hemisphere, collected using the SOD mass-downloader tool and IRIS Wilber3 tool  
282 (289 observations from South Sandwich Islands to Alaska and 741 observations from other  
283 high latitude events observed in Antarctica). These events were recorded at networks: YT07,  
284 ZM07, 2C, AI, AU, ER, G, GE, II, IU, PS, SY, C, 9G, ID.

285  
286 Locations and arrival times for events before and after 2009 are from the EHB<sup>44</sup> and ISC  
287 catalogues, respectively. We removed the linear trend and mean from vertical component  
288 data, deconvolved the instrument response, and differentiated to velocity. Data were  
289 bandpass filtered between 0.4-2.0 Hz, and the Hilbert transform was applied to take account  
290 of the phase shift between PKPab and PKPdf. We manually picked phase onsets relative to  
291 predicted times from the 1D reference model ak135<sup>45</sup> after applying ellipticity corrections<sup>46</sup>.  
292 PKPdf and PKPbc are picked on the untransformed data, while PKPab is picked on the Hilbert  
293 transformed data. We classified picks based on the clarity of the signal onset, and the  
294 prominence of the signal in the unfiltered trace. Following picking and classification, we  
295 retained 614 and 416 highest quality differential PKPab-df and PKPbc-df travel times,  
296 respectively, measured with respect to ak135 (all data are shown, split by quality, in  
297 Extended Data Fig. 2). These new measurements, combined with the existing catalogues  
298 mentioned above yield 3558 and 1586 high quality PKPab-df and PKPbc-df measurements,  
299 respectively. We only use the high-quality data for all plots and calculations in this paper.

300  
301 Attributing the entire travel-time anomaly to structure in the IC, we convert travel times to  
302 velocity anomalies relative to 1D model ak135<sup>45</sup> as:  $-\frac{dT}{T_{ic}} = \frac{dv}{v}$ , where  $T_{ic}$  and  $v$  are reference  
303 travel times and velocities in the IC, respectively. This accounts for the difference in path  
304 length between the shallow and more deeply travelling waves. We construct cylindrically  
305 symmetric models of anisotropy, in which the perturbation to a spherically symmetric  
306 model<sup>47</sup> is expressed as:

307

308 
$$\frac{\delta v}{v} = a + b \cos^2 \xi + c \cos^4 \xi \quad (S1)$$

309

310 where  $v$  and  $\delta v$  represent the reference velocity and velocity perturbations, respectively  
311 and  $\xi$  is the angle of the ray path direction at the bottoming point of the ray with respect to  
312 Earth's rotation axis. We determine the coefficients  $a$ ,  $b$ , and  $c$  (which can depend on depth  
313 and location, depending on the model considered) by fitting our data with an L1-norm to  
314 account for outliers. The apparent IC velocity anomaly will be the integrated effect of the  
315 velocity anomalies along the raypath in the inner core.

316

317 In order to best illustrate the hemispherical differences, we update hemisphere boundaries  
318 by grid searching for the location of the western boundary of the western hemisphere. We  
319 hold the eastern boundary fixed to that previously found<sup>10</sup> as our dataset has limited  
320 coverage in this region, while the previous study was designed to sample the eastern  
321 boundary. Seeking to test the model of an IC with hemispherical and depth dependent  
322 anisotropy, we split the data into two hemispheres described by the candidate boundaries  
323 and fit models of velocity anomaly as a function of distance to the polar data ( $\xi \leq 15^\circ$ ). Only  
324 the polar data shows significant hemisphericity, thus we exclude higher  $\xi$  data to avoid  
325 biasing the fit with data with little resolving power. We seek to minimise the combined misfit  
326 to the two straight lines (Extended Data Fig. 6). Hemispheres are assigned based on the  
327 longitude of the turning point of the ray, an approximation that works well for polar data,  
328 but for equatorial data leads to smearing of hemispherical differences together. However,  
329 since equatorial data do not show significant differences between hemispheres this  
330 approximation is not problematic. The western boundary of the western hemisphere  
331 produces equal fits to the data when located between  $-166^\circ$  E and  $-159^\circ$  E, with a very sharp  
332 falloff in  $R^2$  at locations  $< -166^\circ$  E or  $> -153^\circ$  E. While we simplify the boundary to a line of  
333 constant longitude, we cannot rule out a bent western boundary<sup>48</sup>. When we repeat this test  
334 with the less-polar data,  $\xi < 35^\circ$ , the best fitting hemisphere locations are similar with a sharp  
335 falloff at  $< -153^\circ$  E.

336

337 To determine the robustness of the resolved gradients of velocity with depth in each  
338 hemisphere we perform an interaction effect analysis using the data shown in Fig. 2b. We  
339 find that to 95% confidence we cannot reject the null hypothesis that the gradient of the two  
340 hemispheres is the same, i.e. the gradient of the two hemispheres is statistically the same. To  
341 determine the robustness of the offset in intercept between the two gradients we perform a  
342 bootstrap resampling of the same data. We find that the second standard deviations about  
343 the bootstrapped means do not overlap between the two hemispheres. We conclude that the  
344 trends of velocity with depth in the two hemispheres have statistically distinct intercepts but  
345 statistically very similar gradients.

346

### 347 **South Sandwich Islands to Alaska anomaly**

348 PKPbc-df and PKPab-df data recorded at stations in Alaska show a spread of travel time  
349 anomalies that do not match the global pattern as a function of  $\xi$  (Extended Data Fig. 3), as  
350 previously reported<sup>37,49,50</sup>. This is especially clear for PKPbc-df measurements that show  
351 travel time anomalies of up to 6 s, in contrast to measurements outside of Alaska of less than  
352 3 s on the most polar paths. This data may be contaminated by the Alaska slab<sup>49</sup>. We thus

353 remove data recorded in Alaska from the analysis presented here, but we keep data from  
354 events in Alaska, which are not affected by the slab and fit the global trends (Extended Data  
355 Fig. 3).

356

### 357 **Geodynamics**

358 It has previously been proposed by different groups that viscous relaxation of topography at  
359 the inner core boundary, caused by differential growth rate of the inner core, may orientate  
360 crystals in the inner core and explain the inner core bulk anisotropy (Extended Data Fig.  
361 10)<sup>11</sup>. Flows in the inner core induced by preferential growth at the equator have a vertical  
362 cylindrical axis of symmetry and tend to align the crystals along this axis close to the center  
363 of the inner core. However, such a model cannot explain the observation of hemispherical  
364 differences in IC anisotropy. Meanwhile, lateral translation caused by either simultaneous  
365 melting and crystallisation on opposite sides of the IC<sup>15,16</sup> or an unstable compositional  
366 gradient<sup>12,14</sup> has been proposed to explain the hemispherical dichotomy in the IC.

367 Here we consider the flows induced by differential growth rate at the inner core boundary,  
368 where the differential growth rate is a sum of two previously studied patterns: preferential  
369 equatorial growth and hemispherical asymmetric growth (Extended Data Fig. 10). We  
370 consider neutral density stratification of the inner core, as it is the only regime in which  
371 deformation occurs at depth<sup>4</sup>. This drastically reduces the parameter space where such a  
372 flow could be observed, as a slightly unstable density stratification develops large-scale  
373 convection<sup>51</sup> and a stable density stratification inhibits radial flows and layers of high  
374 deformation develop near the inner core boundary<sup>13</sup>. As discussed before<sup>4</sup>, preferential  
375 growth at the equator would still develop large-scale flows for stable stratification for large  
376 viscosity values ( $\eta > 10^{18}$  Pa.s) and an age of inner core larger than the diffusive time scale  
377 (0.2-1.5 Ga). The assumption of Yoshida-style convection thus restricts the range of possible  
378 viscosities for the IC.

379 We solve the conservation of momentum equation for an incompressible fluid of constant  
380 viscosity  $\eta$  and constant density  $\rho$  in a spherical shell whose radius increases with time as  
381  $R_{ic}(t) = R_{ic}(\tau_{ic})\sqrt{t/\tau_{ic}}$  from time 0, representing the nucleation of the inner core, to  
382 time  $\tau_{ic}$ , today. The assumption of neutral stratification allows for a complete analytical  
383 solution for the flow for both the equatorial<sup>11</sup> and hemispherical patterns.

384

385 To determine the trajectory of a particle in the inner core, we fix the position of the particle  
386 today (at  $\tau_{ic}$ ) and integrate the trajectory backward in time using GrowYourIC<sup>52</sup>. The  
387 intersection of the trajectory and the ICB in the past corresponds to the time of crystallisation  
388 of the material.

389

390 We output the positions, velocity components, and velocity gradients of the particles with  
391 time and use this to calculate crystal orientations. To obtain a first idea of the deformation  
392 experienced by the particle, we calculate the vonMises equivalent strain rate and its average  
393 over the trajectory for  $t_{\text{crystallisation}} > 0$ .

394

395 In modelling the growth and resulting strain in the inner core, we also test the dependence  
396 of S2 on the preferred IC age and translation rate. We explore translation rates between 0

397 and 0.5 in increment of 0.1 radii of the IC over the age of the IC, IC ages between 0.25 and 1.5  
398 in increments of 0.25, and S2 between 0.2 and 1.0 in increments of 0.2, searching for the  
399 model that best matches the observed anisotropy. Such slow translation rates, which are  
400 lower than the crystallisation rate, require only differential freezing and no melting, unlike  
401 models of fast translation<sup>15,16</sup>. We calculate the core growth and translation for non-  
402 dimensionalised time and IC size. We then scale the model using the radius of the inner core  
403 at the present day (1217.5 km) and the chosen age of the inner core. Thus, we scale the  
404 instantaneous strain rate by the inverse of the IC age ( $1/\tau_{ic}$ ) and the time step ( $dt$ ) by the IC  
405 age ( $dt * \tau_{ic}$ ). Inner core age linearly affects the strain rate, but the maximum total  
406 accumulated strain for all IC ages is equal to S2, thus the value of S2 affects the total  
407 accumulated strain and the strain rate, while IC age only affects the strain rate. For each inner  
408 core age, S2, and translation rate, we use VPSC to calculate the resulting deformation. We  
409 model deformation by dislocation-creep, thus strain-rate and time step have a non-linear  
410 influence on the generation of anisotropy. Comparison of the resultant anisotropy models  
411 with our seismic observations suggest best-fitting ages between 0.5 and 1.5 Ga, depending  
412 on S2, with a translation rate of 0.3 radii over the age of the IC. Since models with  $S2 < 0.4$   
413 generate too little anisotropy to match the data and models with  $S2 \geq 0.8$  require an IC age of  
414 0.25 Ga (which is likely too young<sup>53-55</sup>), we determine reasonable bounds for S2 of  
415  $0.4 \leq S2 \leq 0.6$ , with the age trading off accordingly between 1.5 and 0.5 Ga, respectively.  
416 External constraints on the parameter S2 are poor, but previous work based on outer core  
417 geodynamics considerations<sup>12</sup> has preferred  $S2 = 0.4$ , which is consistent with our preferred  
418 range. The data can be fit by models with ages that are consistent with the range suggested  
419 from paleomagnetic constraints (between 0.5 Ga and 1.3 Ga<sup>38,39</sup>).

420  
421 Anisotropy strength depends on IC age and S2 thus by matching the observed strength of  
422 anisotropy for a given S2 we can estimate IC age. Models with  $S2 = 0.4$  and inner core ages  
423  $> 0.5$  Ga generate strong and localised anisotropy capable of matching our observations.  
424 Models run with inner core ages  $< 0.5$  Ga have maximum anisotropies of less than 6.0%, and  
425 the volume of the IC with maximum anisotropy is very small. These models predict weaker  
426 anisotropy and lower gradients of anisotropy with depth than what we observe. In contrast,  
427 for older inner cores the maximum anisotropy reaches  $\sim 7.0\%$  in places, thus achieves nearly  
428 full alignment of crystals, for which anisotropy would be 7.5%. For  $S2 = 0.6$  inner core ages  
429  $\geq 0.5$  predict strong anisotropy with a maximum anisotropy of  $\sim 7.0\%$  in places, equivalent  
430 to the models with  $S2 = 0.4$  and IC age  $\geq 1.0$  Ga. In fact, for  $S2 = 0.6$  and IC ages  $> 1.0$  Ga, the  
431 models begin to predict anisotropy that is stronger than the observations. Age of the IC also  
432 depends on IC viscosity through its influence on strain rate, but the viscosity is fixed to  $> 10^{18}$   
433 Pa-s by our assumption of Yoshida-style deformation<sup>4</sup>. Alternative solutions to fit the large  
434 anisotropy would be either easier deformation of hcp iron-nickel alloy than in our VPSC  
435 simulation, stronger single crystal anisotropy, or pressure dependence of the single crystal  
436 anisotropy (Extended Data Figure 9). However, both the deformation behaviour and precise  
437 anisotropic pattern of iron and iron alloys at high pressures and temperatures are not well  
438 constrained.

439  
440 We rotate the resulting model of anisotropy about the rotation axis and in the equatorial  
441 plane through  $360^\circ$  in  $10^\circ$  increments and compare the misfit with the data. We thus find  
442 that the best fitting growth direction is from  $120^\circ\text{E}$  towards  $60^\circ\text{W}$ , placing the points of

443 fastest and slowest growth under the Banda Sea and Brazil, respectively. Interestingly, these  
444 are very similar to the foci of growth and melting modelled by <sup>16</sup>, albeit with the opposite  
445 direction of growth.

446

### 447 **Mineral physics**

448 We calculate the anisotropy that would result from a deformation of an IC of a given  
449 composition in the presence of the strain field described above. An important component is  
450 the composition chosen, as anisotropy of the single crystal controls the anisotropy of the  
451 bulk model after deformation. Experimental studies indicate that hexagonally close packed  
452 (hcp) iron is stable at IC conditions<sup>56</sup>, but this is complicated by the presence of lighter  
453 elements in the IC. The body centred cubic (bcc) iron phase may also be stable<sup>57</sup>, depending  
454 on the strain field<sup>58</sup>. First principles calculations estimate the anisotropy of pure single iron  
455 crystals to range from 4.9-7.9% for hcp iron (given as the total range from minimum to  
456 maximum  $dlnV$ ), and up to 14.7% for bcc iron<sup>18,42,59</sup>, and potentially up to 20% near the  
457 melting point of hcp iron<sup>60</sup>, although there is debate over the trends of anisotropy as a  
458 function of pressure and temperature<sup>59,61-64</sup>. The pattern of anisotropy for iron near its  
459 melting point<sup>60</sup> is very different from the observed IC anisotropy. Alloys of iron with  
460 plausible light elements modify the character of anisotropy, but the limited number of  
461 experiments leaves the dependence on pressure and temperature uncertain<sup>20,65-69</sup>. We select  
462 hcp iron-nickel alloy ( $Fe_{93.75}Ni_{6.25}$ )<sup>20</sup> as its pattern of single crystal anisotropy (Extended  
463 Data Fig. 11) is most similar to the observed anisotropy (Extended Data Figs. 3 and 4) and it  
464 is consistent with cosmo-chemical calculations of the core's composition<sup>21</sup>.

465

466 We calculate the development of Crystal Preferred Orientation (CPO) in the presence of the  
467 strain field resulting from our above inner core growth models using the Visco-Plastic Self-  
468 Consistent modelling code (VPSC)<sup>17</sup>. Groups of 1500 particles, representing crystals of hcp  
469 iron-nickel alloy ( $Fe_{93.75}Ni_{6.25}$ ) are generated at the Inner Core Boundary throughout the  
470 growth history of the inner core. Crystal growth at the ICB may cause pre-texturing<sup>70</sup>. We  
471 model particles with an initial solidification pre-texture in which the c-axes of the hcp iron  
472 crystals are oriented in the plane of the ICB, as in previous work<sup>5</sup>. The group of particles  
473 deforms as it is subject to the strain along the tracer path. The deformation is controlled by  
474 the crystal slip systems, for which we use those of hcp iron. Following from a previous study<sup>5</sup>,  
475 we allow slip along the  $\langle c+a \rangle$  pyramidal planes of hcp iron and lock the remaining slip  
476 systems and we set the normalized critically resolved shear stresses to  $\infty$  for the basal  $\langle a \rangle$ ,  
477 prismatic  $\langle a \rangle$ , and pyramidal  $\langle a \rangle$  plane slip systems, and 0.5 for the pyramidal  $\langle c+a \rangle$  plane  
478 slip system. We measure the resultant CPO at the present day.

479

480 CPO developed at each step of the growth model is combined with its respective elastic  
481 tensor to determine the resultant anisotropy. We incorporate estimates of the elastic tensors  
482 resulting from *ab initio* molecular dynamic simulations. For our chosen hcp FeNi alloy,  
483 elastic tensors are only available at 0 K and 360 GPa, and 5500 K and 360 GPa<sup>20</sup>. The  
484 temperature range of the inner core is likely very small – on the order of 30 K<sup>71</sup>. We thus  
485 neglect the pressure and temperature dependence of the elastic constants and calculate the  
486 resultant CPO for  $Fe_{93.75}Ni_{6.25}$  alloy at 5500 K and 360 GPa (Extended Data Fig. 11). The  
487 discrepancy between the observed and predicted anisotropy in the eastern hemisphere

488 (Figure 4a) may result from the single crystal anisotropy being fixed with respect to  
489 pressure, thus not allowing weak enough anisotropy to match the data.

490  
491 We seek to understand the influence of the physical state with depth in the IC on the elastic  
492 tensors. As above, we neglect the temperature dependence given its small impact on elastic  
493 tensors but consider the influence of pressure. Given the limited data for FeNi alloys, we  
494 assess the effects of the pressure dependence of anisotropy using pure Fe, for which there  
495 are data at a range of pressures from *ab initio* calculations<sup>20,59</sup>. Pressure as a function of  
496 radius was extracted from the Preliminary Reference Earth Model (PREM)<sup>72</sup> where the  
497 pressure ranges from 330 GPa at the inner core boundary (ICB) to 364 GPa at the centre of  
498 the Earth. A reference point of 360 GPa and 5500 K was chosen, and the derivatives of  
499 pressure at a constant temperature were determined by a middle difference method using  
500 results from the above-mentioned studies. Elastic constants from the reference point were  
501 then interpolated using a Taylor expansion to the 2<sup>nd</sup> derivative of pressure from the  
502 reference point to the pressure at each location along the geodynamic streamline (Extended  
503 Data Fig. 9). We find that at pressures of the ICB, pure hcp Fe would show weaker anisotropy  
504 of 5% and stronger anisotropy of 7% at the centre of the IC.

505  
506 To predict travel time anomalies generated by the modelled anisotropy, we trace rays  
507 through 1D velocity model ak135 between the ICB piercing points for each of our  
508 observations using TauP<sup>73</sup>, assuming propagation along the theoretical raypath in the 1D  
509 model. We interpolate the anisotropy model to a 50×50×50 km grid spacing and interpolate  
510 the ray to increase spatial sampling. For each ray segment, we find the anisotropy at the  
511 nearest model location, measure the  $\xi$  angle of the ray segment, calculate the velocity  
512 anomaly for that  $\xi$  angle using Christoffel's equation, and calculate the resulting travel time  
513 anomaly given the length of the ray segment. We sum the travel time anomalies over the ray  
514 to find the total predicted anomaly for each path through the anisotropy model. We calculate  
515 the variance reduction between the observed and predicted travel time anomalies for the  
516 most polar data,  $\xi < 15^\circ$ , without separating hemispheres.

517 **Data availability statement**

518 The seismic travel time data that support the findings of this study (Figures 1, 2, 4, and  
519 Extended Data Figures 2, 3, 4, 6 and 8) are available from the corresponding author upon  
520 request. Raw seismic waveform data and metadata are accessible through the facilities of  
521 IRIS Data Services, and specifically the IRIS Data Management Center. IRIS Data Services are  
522 funded through the Seismological Facilities for the Advancement of Geoscience and  
523 EarthScope (SAGE) Proposal of the National Science Foundation under Cooperative  
524 Agreement EAR-1261681. The EHB On-line Bulletins are available from the International  
525 Seismological Centre (ISC), for access to the EHB and, <http://www.isc.ac.uk>, Internatl.  
526 Seismol. Cent., Thatcham, United Kingdom, 2015.

527

528 **Acknowledgements**

529 **Funding:** Daniel A Frost and Barbara Romanowicz acknowledge support from NSF (grants  
530 EAR-1135452 and EAR-1829283). Marine Lasbleis acknowledges  
531 support from the European Union's Horizon 2020 research and innovation program under  
532 the Marie Skłodowska-Curie Grant Agreement No. 795289. Brian Chandler acknowledges  
533 support from NSF (grant EAR 1343908) and DOE (grant DE-FG02-05ER15637).

534

535 **Author contributions:** All authors contributed to project design, methodology  
536 development, model conceptualization and manuscript preparation. DAF was responsible  
537 for seismic data curation and formal analysis and wrote the first draft of the paper. ML  
538 contributed to the geodynamic modeling and BC provided the mineral physics input. DAF  
539 and BR coordinated the project.

540 **Competing interests:** No authors have any known competing interests.

541

542 **References**

- 543 1. Poupinet, G., Pillet, R. & Souriau, A. Possible heterogeneity of the Earth's core  
544 deduced from PKIKP travel times. *Nature* **305**, 294–206 (1983).
- 545 2. Morelli, A., Dziewonski, A. M. & Woodhouse, J. H. Anisotropy of the inner core  
546 inferred from PKIKP travel times. *Geophys. Res. Lett.* **13**, 1545–1548 (1986).
- 547 3. Woodhouse, J. H., Giardini, D. & Li, X. -D. Evidence for inner core anisotropy from free  
548 oscillations. *Geophys. Res. Lett.* **13**, 1549–1552 (1986).
- 549 4. Lasbleis, M. & Deguen, R. Building a regime diagram for the Earth's inner core. *Phys.*  
550 *Earth planet. Int.* **247**, 80–93 (2015).
- 551 5. Lincot, A., Cardin, P., Deguen, R. & Merkel, S. Multiscale model of global inner-core  
552 anisotropy induced by hcp alloy plasticity. *Geophys. Res. Lett.* **43**, 1084–1091 (2016).
- 553 6. Tanaka, S. & Hamaguchi, H. Degree one heterogeneity and hemispherical variation of  
554 anisotropy in the inner core from PKP (BC)- PKP (DF) times. *J. Geophys. Res.* **102**,  
555 2925–2938 (1997).
- 556 7. Creager, K. C. Large-scale variations in inner core anisotropy. *J. Geophys. Res.* **104**,  
557 23127–23139 (1999).
- 558 8. Irving, J. C. E. & Deuss, A. Hemispherical structure in inner core velocity anisotropy. *J.*  
559 *Geophys. Res.* **116**, 1–17 (2011).
- 560 9. Lythgoe, K. H., Deuss, A., Rudge, J. F. & Neufeld, J. A. Earth's inner core: Innermost  
561 inner core or hemispherical variations? *Earth Planet. Sci. Lett.* **385**, 181–189 (2014).
- 562 10. Irving, J. C. E. Imaging the inner core under Africa and Europe. *Phys. Earth planet. Int.*

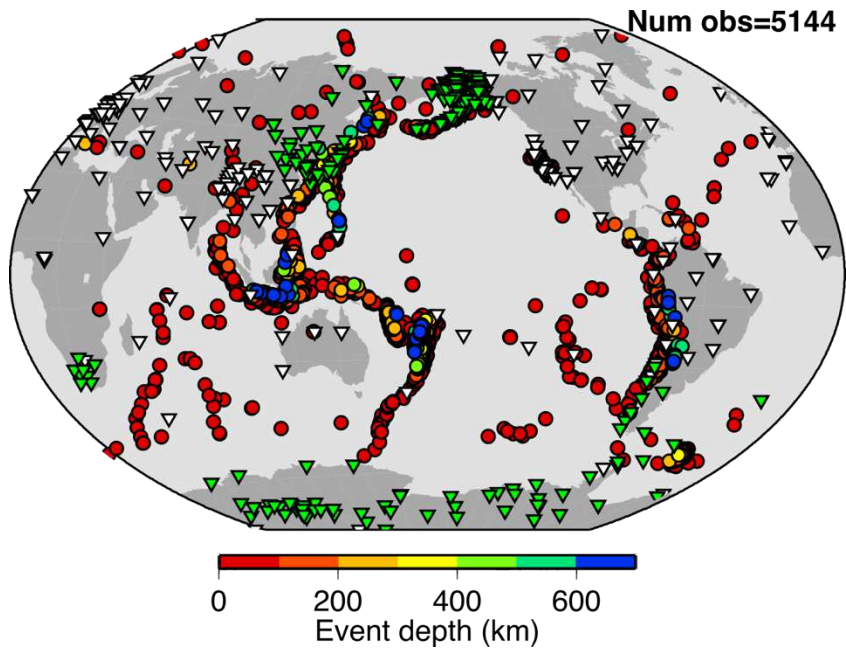
- 563 **254**, 12–24 (2016).
- 564 11. Yoshida, S., Sumita, I. & Kumazawa, M. Growth model of the inner core coupled with  
565 the outer core dynamics and the resulting elastic anisotropy. *J. Geophys. Res.* **101**,  
566 28085–28103 (1996).
- 567 12. Aubert, J., Amit, H., Hulot, G. & Olson, P. Thermochemical flows couple the Earth's  
568 inner core growth to mantle heterogeneity. *Nature* **454**, 758–761 (2008).
- 569 13. Deguen, R., Cardin, P., Merkel, S. & Lebensohn, R. A. Texturing in Earth's inner core  
570 due to preferential growth in its equatorial belt. *Phys. Earth planet. Int.* **188**, 173–184  
571 (2011).
- 572 14. Deguen, R., Alboussière, T. & Labrosse, S. Double-diffusive translation of Earth's inner  
573 core. *Geophys. J. Int.* **214**, 88–107 (2018).
- 574 15. Alboussière, T., Deguen, R. & Melzani, M. Melting-induced stratification above the  
575 Earth's inner core due to convective translation. *Nature* **466**, 744–747 (2010).
- 576 16. Monnereau, M., Calvet, M., Margerin, L. & Souriau, A. Lopsided growth of Earth's  
577 inner core. *Science (80-. )*. **328**, 1014–1017 (2010).
- 578 17. Lebensohn, R. A. & Tomé, C. N. A self-consistent anisotropic approach for the  
579 simulation of plastic deformation and texture development of polycrystals:  
580 Application to zirconium alloys. *Acta Met. Mater.* **41**, 2611–2624 (1993).
- 581 18. Belonoshko, A. B. *et al.* Origin of the low rigidity of the earth's inner core. *Science (80-.*  
582 *)*. **316**, 1603–1605 (2007).
- 583 19. Lincot, A., Merkel, S. & Cardin, P. Is inner core seismic anisotropy a marker for plastic  
584 flow of cubic iron? *Geophys. Res. Lett.* **42**, 1326–1333 (2015).
- 585 20. Martorell, B., Brodholt, J., Wood, I. G. & Vočadlo, L. The effect of nickel on the  
586 properties of iron at the conditions of Earth's inner core: Ab initio calculations of  
587 seismic wave velocities of Fe-Ni alloys. *Earth Planet. Sci. Lett.* **365**, 143–151 (2013).
- 588 21. McDonough, W. F. & Sun, S. s. The composition of the Earth. *Chem. Geol.* **120**, 223–  
589 253 (1995).
- 590 22. Miyagi, L. *et al.* In situ phase transformation and deformation of iron at high pressure  
591 and temperature. *J. Appl. Phys.* **104**, (2008).
- 592 23. Merkel, S., Gruson, M., Wang, Y., Nishiyama, N. & Tomé, C. N. Texture and elastic  
593 strains in hcp-iron plastically deformed up to 17.5GPa and 600K: Experiment and  
594 model. *Model. Simul. Mater. Sci. Eng.* **20**, (2012).
- 595 24. Frost, D. A. & Romanowicz, B. On the orientation of the fast and slow directions of  
596 anisotropy in the deep inner core. *Phys. Earth Planet. Inter.* **286**, 101–110 (2019).
- 597 25. Garcia, R. & Souriau, A. Inner core anisotropy and heterogeneity level. *Geophys. Res.*  
598 *Lett.* **27**, 3121–3124 (2000).
- 599 26. Frost, D. A. & Romanowicz, B. Constraints on Inner Core Anisotropy Using Array  
600 Observations of P'P'. *Geophys. Res. Lett.* **44**, 10,878–10,886 (2017).
- 601 27. Romanowicz, B., Li, X. D. & Durek, J. Anisotropy in the inner core: Could it be due to  
602 low-order convection? *Science (80-. )*. **274**, 963–966 (1996).
- 603 28. Irving, J. C. E. & Deuss, A. Stratified anisotropic structure at the top of Earth's inner  
604 core: A normal mode study. *Phys. Earth planet. Int.* **186**, 59–69 (2011).
- 605 29. Bréger, L., Romanowicz, B. & Rousset, S. New constraints on the structure of the  
606 inner core from P'P'. *Geophys. Res. Lett.* **27**, 2781–2784 (2000).
- 607 30. Yu, S. & Garnero, E. J. Ultralow Velocity Zone Locations: A Global Assessment.  
608 *Geochem. Geophys. Geosyst.* **19**, 396–414 (2018).

- 609 31. Ritterbex, S. & Tsuchiya, T. Viscosity of hcp iron at Earth's inner core conditions from  
610 density functional theory. *Sci. Rep.* **10**, 2–5 (2020).
- 611 32. Torsvik, T. H., Smethurst, M. A., Burke, K. & Steinberger, B. Large igneous provinces  
612 generated from the margins of the large low-velocity provinces in the deep mantle.  
613 *Geophys. J. Int.* **167**, 1447–1460 (2006).
- 614 33. Dziewonski, A. M., Lekic, V. & Romanowicz, B. A. Mantle Anchor Structure: An  
615 argument for bottom up tectonics. *Earth Planet. Sci. Lett.* **299**, 69–79 (2010).
- 616 34. Greff-Lefftz, M. & Besse, J. Paleo movement of continents since 300Ma, mantle  
617 dynamics and large wander of the rotational pole. *Earth Planet. Sci. Lett.* **345–348**,  
618 151–158 (2012).
- 619 35. Ballmer, M. D., Houser, C., Hernlund, J. W., Wentzcovitch, R. M. & Hirose, K.  
620 Persistence of strong silica-enriched domains in the Earth's lower mantle. *Nat.*  
621 *Geosci.* **10**, 236–240 (2017).
- 622 36. Aubert, J., Finlay, C. C. & Fournier, A. Bottom-up control of geomagnetic secular  
623 variation by the Earth's inner core. *Nature* **502**, 219–223 (2013).
- 624 37. Tkalčić, H. Large variations in travel times of mantle-sensitive seismic waves from  
625 the South Sandwich Islands: Is the Earth's inner core a conglomerate of anisotropic  
626 domains? *Geophys. Res. Lett.* **37**, 1–6 (2010).
- 627 38. Biggin, A. J. *et al.* Palaeomagnetic field intensity variations suggest Mesoproterozoic  
628 inner-core nucleation. *Nature* **526**, 245–248 (2015).
- 629 39. Bono, R. K., Tarduno, J. A., Nimmo, F. & Cottrell, R. D. Young inner core inferred from  
630 Ediacaran ultra-low geomagnetic field intensity. *Nat. Geosci.* **12**, 143–147 (2019).
- 631 40. Tkalčić, H., Romanowicz, B. & Houy, N. Constraints on D'' structure using PKP (AB–  
632 DF), PKP (BC–DF) and PcP–P traveltimes data from broad-band records. *Geophys. J.*  
633 *Int.* **148**, 599–616 (2002).
- 634 41. Cao, A. & Romanowicz, B. Test of the innermost inner core models using broadband  
635 PKIKP travel time residuals. *Geophys. Res. Lett.* **34**, 1–5 (2007).
- 636 42. Romanowicz, B. *et al.* Seismic anisotropy in the Earth's innermost inner core: testing  
637 structural models against mineral physics predictions. *Geophys. Res. Lett.* 93–100  
638 (2015). doi:10.1002/2015GL066734
- 639 43. Tkalčić, H., Young, M., Muir, J. B., Davies, D. R. & Mattesini, M. Strong, Multi-Scale  
640 Heterogeneity in Earth's Lowermost Mantle. *Sci. Rep.* **5**, 1–8 (2015).
- 641 44. Robert Engdahl, E., Van Hilst, R. Der & Buland, R. Global teleseismic earthquake  
642 relocation with improved travel times and procedures for depth determination. *Bull.*  
643 *Seismol. Soc. Am.* **88**, 722–743 (1998).
- 644 45. Kennett, B. L. N., Engdahl, E. R. & Buland, R. Constraints on seismic velocities in the  
645 Earth from traveltimes. *Geophys. J. Int.* **122**, 108–124 (1995).
- 646 46. Kennett, B. L. N. & Gudmundsson, O. Ellipticity corrections for seismic phases.  
647 *Geophys. J. Int.* **127**, 40–48 (1996).
- 648 47. Creager, K. C. Anisotropy of the inner core from differential travel times of the  
649 phases\nPKP and PKIKP. *Nature* **356**, 309–314 (1992).
- 650 48. Yu, W. che *et al.* The inner core hemispheric boundary near 180 °W. *Phys. Earth*  
651 *planet. Int.* **272**, 1–16 (2017).
- 652 49. Romanowicz, B., Tkalčić, H. & Bréger, L. On the Origin of Complexity in PKP Travel  
653 Time Data. *Earth's Core Dyn. Struct. Rotat.* 31–44 (2003). doi:10.1029/GD031p0031
- 654 50. Romanowicz, B. & Wenk, H. R. Anisotropy in the deep Earth. *Phys. Earth planet. Int.*

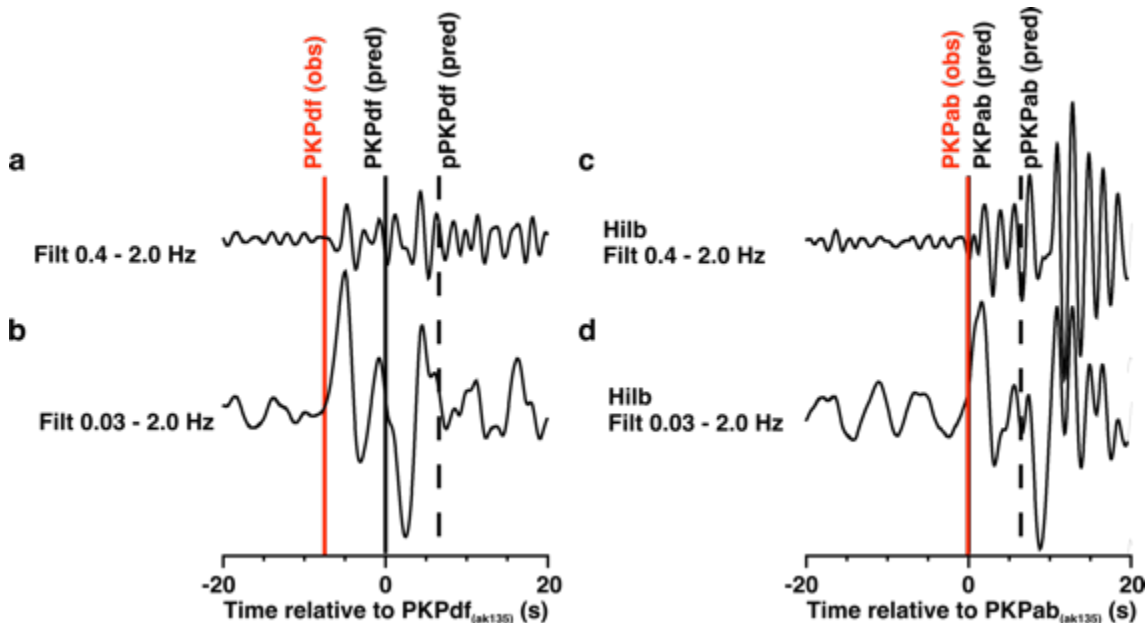
- 655           **269**, 58–90 (2017).
- 656 51. Deguen, R., Olson, P. & Reynolds, E. F-layer formation in the outer core with  
657 asymmetric inner core growth. *Comptes rendus - Geosci.* **346**, 101–109 (2014).
- 658 52. Lasbleis, M., Waszek, L. & Day, E. A. GrowYourIC: A Step Toward a Coherent Model of  
659 the Earth's Inner Core Seismic Structure. *Geochem. Geophys. Geosyst.* **18**, 4016–4026  
660 (2017).
- 661 53. Pozzo, M., Davies, C., Gubbins, D. & Alfè, D. Thermal and electrical conductivity of iron  
662 at Earth's core conditions. *Nature* **485**, 355–358 (2012).
- 663 54. Dobson, D. Earth's core problem. *Nature* **534**, 45 (2016).
- 664 55. Ohta, K., Kuwayama, Y., Hirose, K., Shimizu, K. & Ohishi, Y. Experimental  
665 determination of the electrical resistivity of iron at Earth's core conditions. *Nature*  
666 **534**, 95–98 (2016).
- 667 56. Tateno, S., Hirose, K., Ohishi, Y. & Tatsumi, Y. The Structure of Iron in Earth's Inner  
668 Core. *Science (80-. )*. **330**, 359–362 (2010).
- 669 57. Belonoshko, A. B. *et al.* Stabilization of body-centred cubic iron under inner-core  
670 conditions. *Nat. Geosci.* **10**, 312–316 (2017).
- 671 58. Vočadlo, L. *et al.* The stability of bcc-Fe at high pressures and temperatures with  
672 respect to tetragonal strain. *Phys. Earth planet. Int.* **170**, 52–59 (2008).
- 673 59. Vočadlo, L., Dobson, D. P. & Wood, I. G. Ab initio calculations of the elasticity of hcp-Fe  
674 as a function of temperature at inner-core pressure. *Earth Planet. Sci. Lett.* **288**, 534–  
675 538 (2009).
- 676 60. Martorell, B., Vočadlo, L., Brodholt, J. & Wood, I. G. Strong premelting effect in the  
677 elastic properties of hcp-Fe under inner-core conditions. *Science (80-. )*. **342**, 466–  
678 468 (2013).
- 679 61. Steinle-Neumann, G., Stixrude, L., Cohen, R. E. & Gülseren, O. Elasticity of iron at the  
680 temperature of the Earth's inner core. *Nature* **413**, 57–60 (2001).
- 681 62. Gannarelli, C. M. S., Alfè, D. & Gillan, M. J. The particle-in-cell model for ab initio  
682 thermodynamics: Implications for the elastic anisotropy of the Earth's inner core.  
683 *Phys. Earth planet. Int.* **139**, 243–253 (2003).
- 684 63. Gannarelli, C. M. S., Alfè, D. & Gillan, M. J. The axial ratio of hcp iron at the conditions  
685 of the Earth's inner core. *Phys. Earth planet. Int.* **152**, 67–77 (2005).
- 686 64. Antonangeli, D., Merkel, S. & Farber, D. L. Elastic anisotropy in hcp metals at high  
687 pressure and the sound wave anisotropy of the Earth's inner core. *Geophys. Res. Lett.*  
688 **33**, 1–5 (2006).
- 689 65. Wu, X., Mookherjee, M., Gu, T. & Qin, S. Elasticity and anisotropy of iron-nickel  
690 phosphides at high pressures. *Geophys. Res. Lett.* **38**, 10–13 (2011).
- 691 66. Mookherjee, M. Elasticity and anisotropy of Fe<sub>3</sub>C at high pressures. *Am. Mineral.* **96**,  
692 1530–1536 (2011).
- 693 67. Mookherjee, M. *et al.* High-pressure behavior of iron carbide (Fe<sub>7</sub>C<sub>3</sub>) at inner core  
694 conditions. *Geophys. J. Int.* **116**, (2011).
- 695 68. Martorell, B., Wood, I. G., Brodholt, J. & Vočadlo, L. The elastic properties of hcp-  
696 Fe<sub>1-x</sub>Six at Earth's inner-core conditions. *Earth Planet. Sci. Lett.* **451**, 89–96 (2016).
- 697 69. Li, Y., Vočadlo, L., Alfè, D. & Brodholt, J. Mg partitioning between solid and liquid iron  
698 under the Earth's core conditions. *Phys. Earth planet. Int.* **274**, 218–221 (2018).
- 699 70. Bergman, M. I. Measurements of electric anisotropy due to solidification texturing  
700 and the implications for the Earth's inner core. *Nature* **389**, 60–63 (1997).

- 701 71. Stacey, F. D. & Davis, P. M. High pressure equations of state with applications to the  
702 lower mantle and core. *Phys.* **142**, 137–184 (2004).
- 703 72. Dziewonski, A. M. & Anderson, D. L. Preliminary reference Earth model. *Phys.* **25**,  
704 297–356 (1981).
- 705 73. Crotwell, H. P., Owens, T. J. & Ritsema, J. The TauP Toolkit: Flexible Seismic Travel-  
706 time and Ray-path Utilities. *Seismol. Res. Lett.* **70**, 154–160 (1999).
- 707 74. Waszek, L., Irving, J. & Deuss, A. Reconciling the hemispherical structure of Earth's  
708 inner core with its super-rotation. *Nat. Geosci.* **4**, 264–267 (2011).
- 709  
710

711 Extended Data  
 712 List of Extended Data figures:  
 713 Extended Data Figures 1-11  
 714

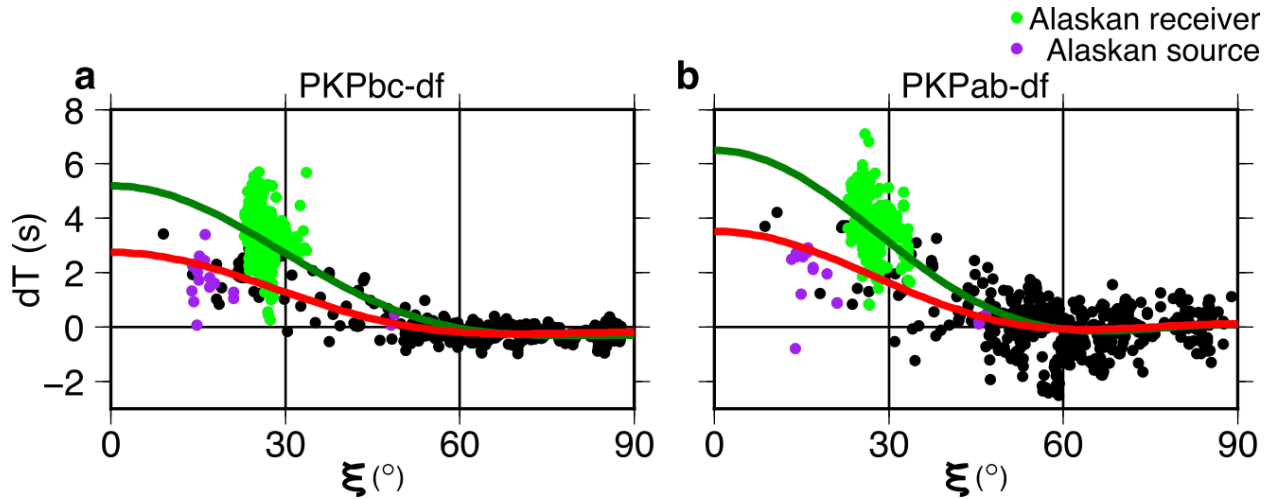


715  
 716 **Extended Data Figure 1:** Locations of sources (circles) and receivers (triangles) used in this  
 717 study. Stations with newly acquired data are shown in green.  
 718

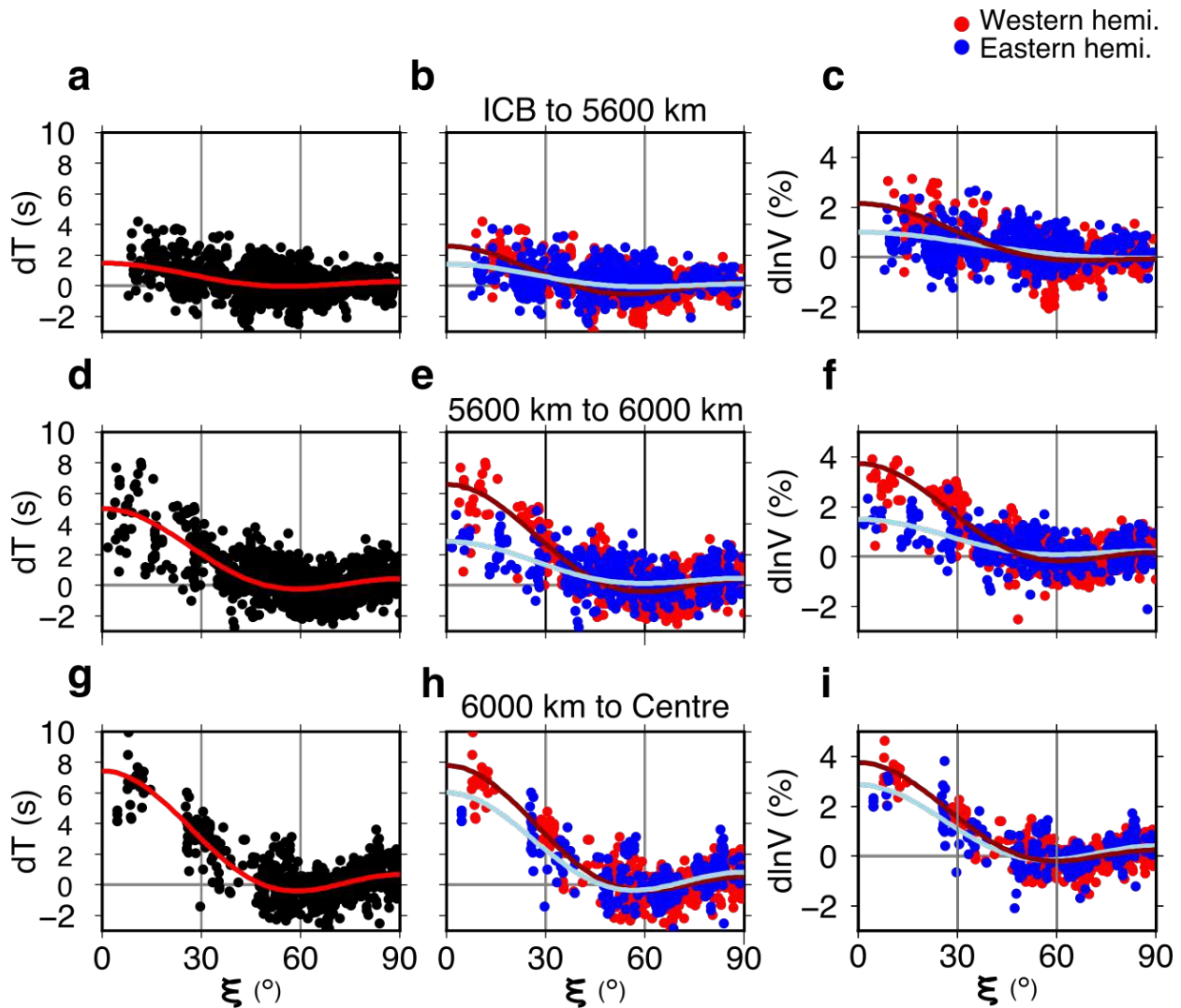


719  
 720 **Extended Data Figure 2:** Example waveforms of (left) PKPdf and (right) PKPab for a M6.0  
 721 event in Baffin Bay on 2009/07/07 observed at station P124 in Antarctica. Waveforms are  
 722 aligned on the predicted arrival time of the respective phases. Waveforms are shown as (a-  
 723 c) broadly filtered at 0.03-2 Hz, (b-d) narrowly filtered at 0.4-2.0 Hz. In (c) and (d)  
 724 waveforms have been Hilbert transformed. Measured arrival times are shown as red lines.

725 Predicted arrivals (in model ak135 with ellipticity corrections) are shown by black solid and  
726 dashed lines for direct and depth phases, respectively.  
727

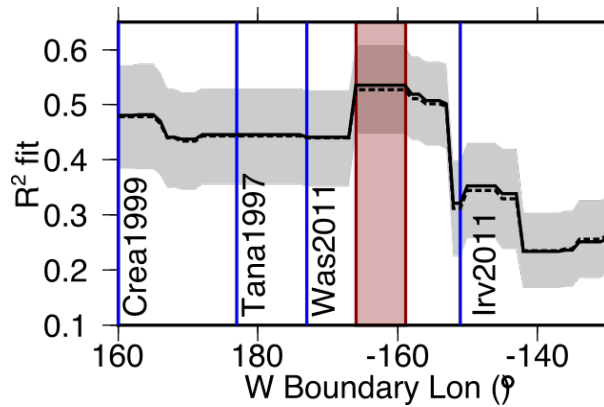


728 **Extended Data Figure 3: Differential travel time anomalies for western hemisphere**  
729 **data turning within 450 km of the ICB with respect to model ak135, as a function of**  
730 **angle  $\xi$  and data quality.** High quality travel time anomalies of (a) PKPbc-df and (b) PKPac-  
731 df phase pairs showing that observations at stations in Alaska (green) do not fit the global  
732 pattern, while observations from sources in Alaska (purple) do. Anisotropy curves are  
733 calculated using equation S1, assuming constant cylindrical anisotropy through the inner  
734 core, for all data (green curve) and all data except that recorded in Alaska (red curve).  
735  
736  
737



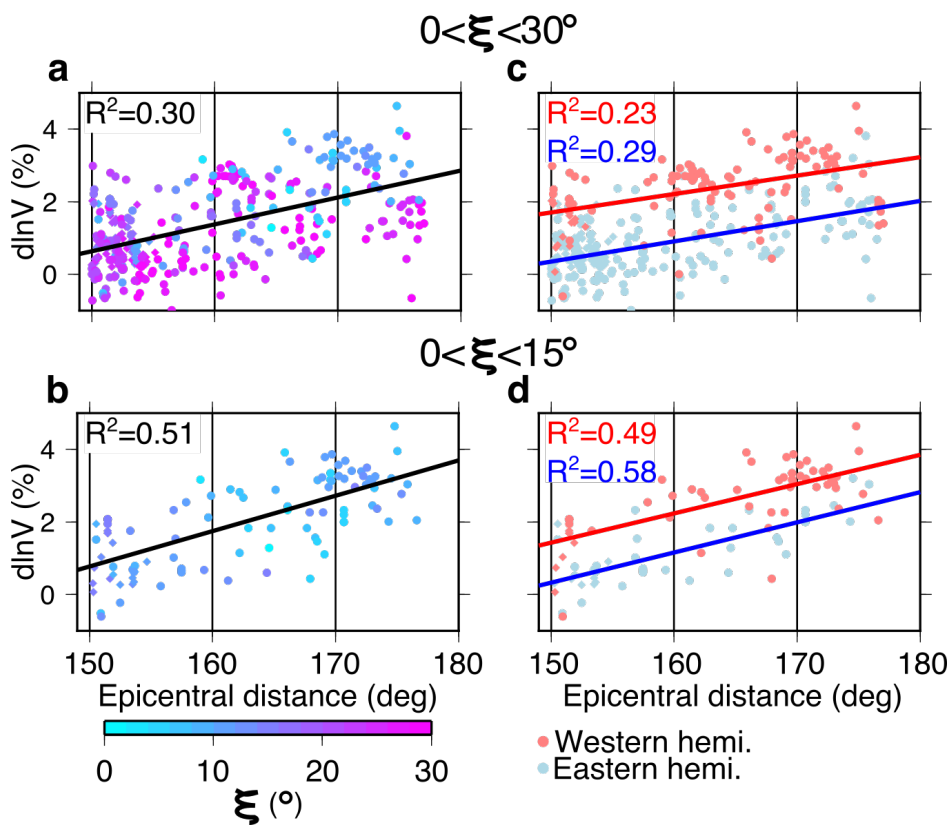
738  
 739  
 740  
 741  
 742  
 743  
 744  
 745  
 746  
 747

**Extended Data Figure 4:** PKPbc-df and PKPab-df travel time anomalies and effective velocity anomalies (excluding the data recorded at stations in Alaska) as a function of angle  $\xi$  with respect to the rotation axis, separated by ray turning depth for **(a, b, and c)** ICB to 5600 km, **(d, e, and f)** 5600 km to 6000 km, and **(g, h, and i)** 6000 km to Earth's centre. **(a, d, g)**: All travel time anomalies. **(b, e, h)** Travel time anomalies split into data turning in the western (red) and eastern (blue) hemispheres. **(c, f, i)** Effective velocity anomalies in the IC split by hemisphere. The WH western boundary is set at  $-159^\circ$  E, and the WH eastern boundary is set at  $40^\circ$  E, as explained in Extended Data Figure 5.



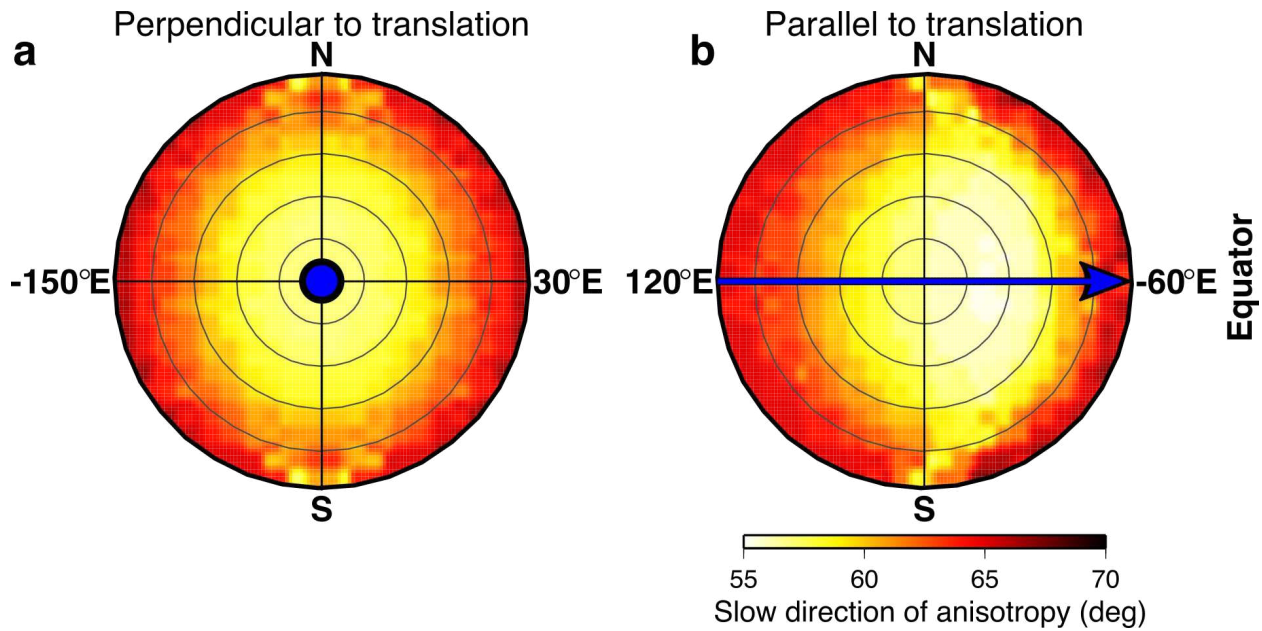
748  
749  
750  
751  
752  
753  
754  
755  
756  
757  
758  
759  
760

**Extended Data Figure 5:** Best fit of WH western boundary locations calculated using polar data ( $\xi < 15^\circ$ ) and excluding data from stations in Alaska. Black solid line marks the  $R^2$  fit and red region describes the region of highest  $R^2$ , most likely containing the location of the boundary, which runs between  $-166^\circ$  E and  $-159^\circ$  E.  $R^2$  drops sharply at  $< -166^\circ$  E and  $> -153^\circ$  E. Black dashed line and grey shading show the mean and standard deviation of  $R^2$  values for 200 bootstrap resamples. The eastern boundary is fixed at  $40^\circ$  E, following the result of Irving (2016). Western boundary locations from previous studies are marked in blue: Tanaka & Hamaguchi 1997<sup>6</sup>; Creager 1999<sup>7</sup>; Waszek et al. 2011<sup>74</sup>; Irving & Deuss 2011<sup>8</sup>; while that of Lythgoe et al. 2014<sup>9</sup> plots outside of the region shown.

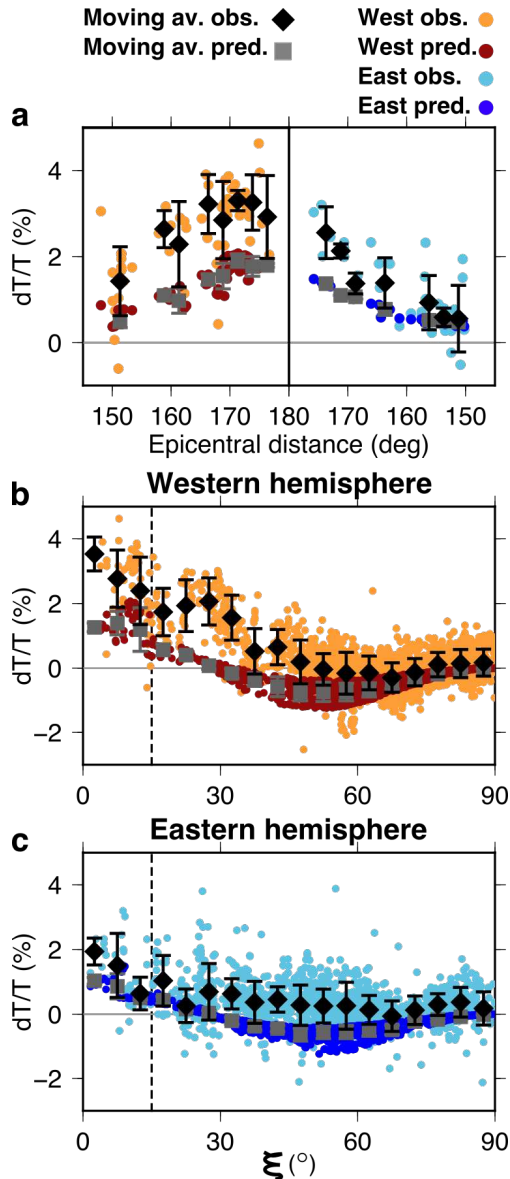


761

762 **Extended Data Figure 6:** Effective velocity anomaly in the IC as a function of epicentral  
 763 distance for  $\xi$  in the range (a and c) 0 to 30°, and (b and d) 0 to 15°. Left panels show data  
 764 coloured by  $\xi$ , and right panels show data split into those turning in the eastern (blue) and  
 765 western (red) hemispheres. The western hemisphere is defined as between -159° E and 40°  
 766 E, as explained in Extended Data Figure 5. The linear trend with distance, solid line, is  
 767 particularly clear for the most polar data (c and f), indicating increasing anisotropy with  
 768 depth.  
 769  
 770

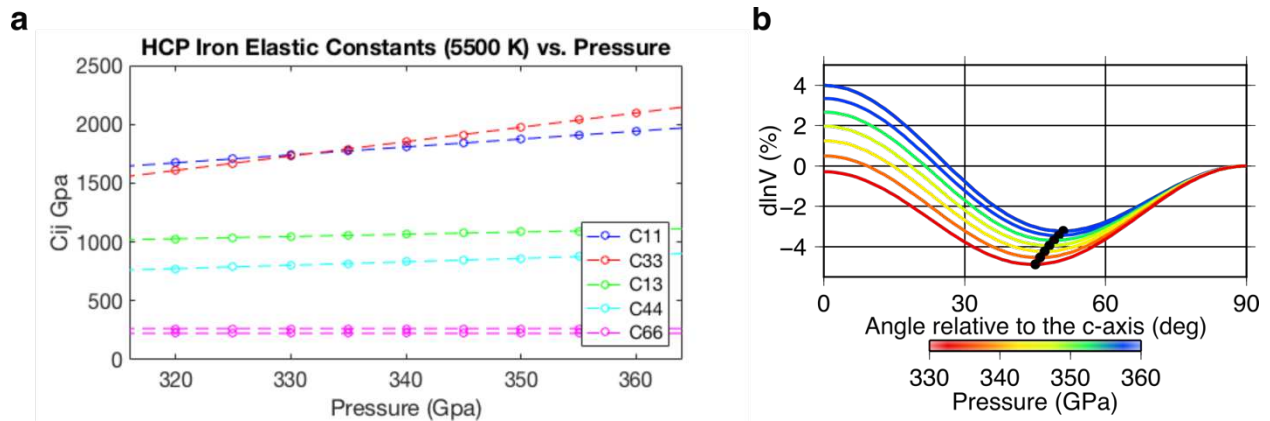


771 **Extended Data Figure 7.** Slow directions of anisotropy in our final model (Fig. 3), measured  
 772 relative to the rotation (N-S) axis in the (a) plane perpendicular to the direction of  
 773 translation (blue arrow coming out of plane), and (b) plane parallel to the direction of  
 774 translation (blue arrow) from the left (east) to right (west) of the figure, respectively.  
 775  
 776  
 777

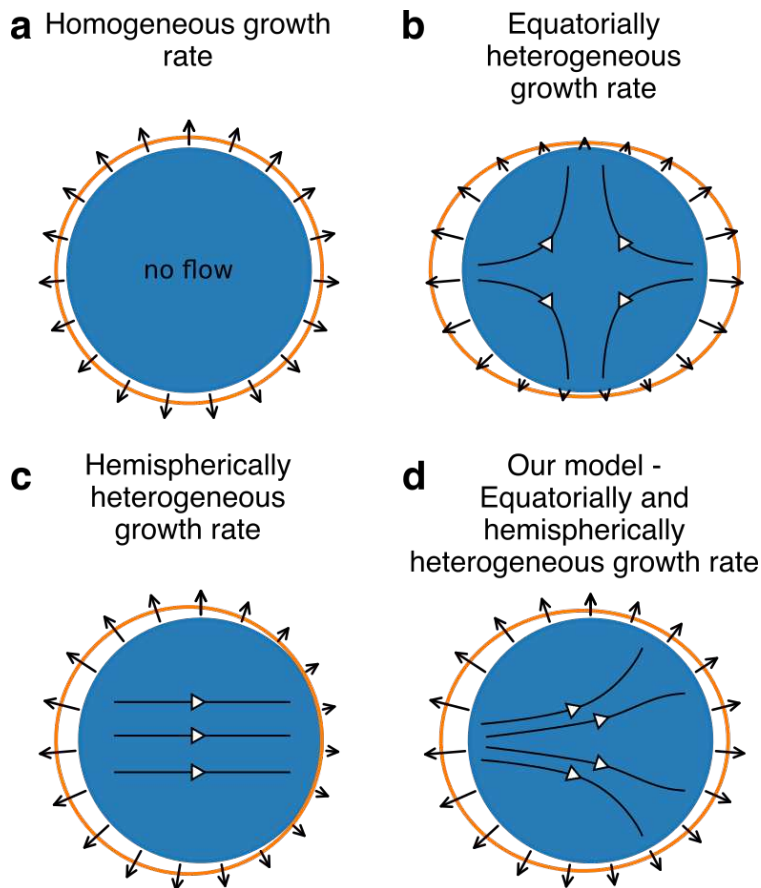


778  
779  
780  
781  
782  
783  
784  
785  
786  
787  
788

**Extended Data Figure 8: Predicted versus observed PKP velocity anomalies for pure hcp Fe.** Predicted (dark blue and red dots and with mean as grey squares) and observed (light blue and orange dots and with mean as black diamonds) effective velocity anomalies as a function of (a) epicentral distance for data with  $\xi \leq 15^\circ$ , marked by dashed line in b and c, and as a function of  $\xi$  in the (b) western and (c) eastern hemispheres. Error bars for the data show the mean and one standard deviation at  $2.5^\circ$  and  $5^\circ$  increments for panels a, and b and c, respectively. We use the elastic tensor for pure HCP Fe at 5500 K and 360 GPa<sup>68</sup>, an age of 0.5 Ga, and a translation rate of 0.3 radii over the age of the IC. Variance reduction for the data with  $\xi < 15^\circ$  is 73% compared to 93% for our model with Fe<sub>93.25</sub>Ni<sub>6.75</sub>.

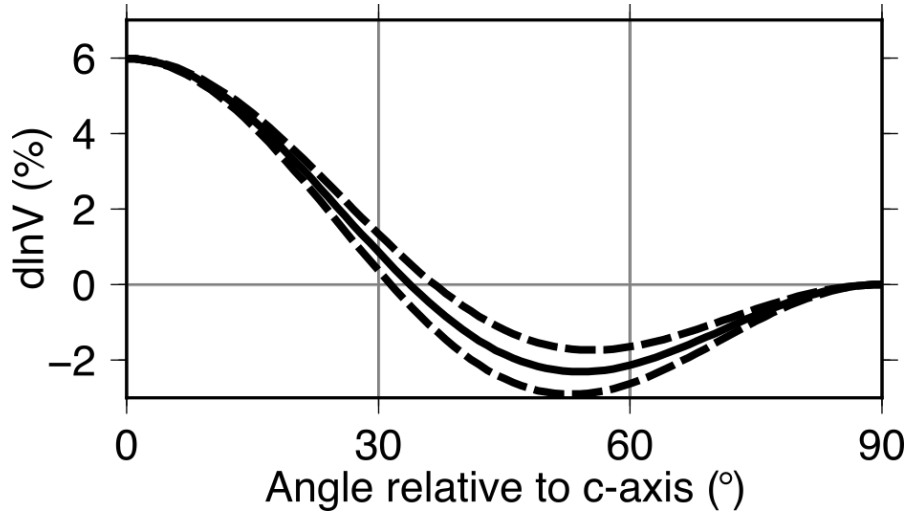


789  
 790 **Extended Data Figure 9:** (a) Elastic constants for hcp iron as a function of pressure  
 791 calculated from the reference position at 360 GPa and 5500 K, extrapolated using results  
 792 from several calculations<sup>59,68</sup> at 5500 K and 316 GPa, and 5500 K and 360 GPa. (b) Resultant  
 793 anisotropy across the pressure range of the inner core. Direction of minimum velocity  
 794 anomaly is marked by black circles. The orientation of the minimum anisotropy moves  
 795 towards higher  $\xi$  values (more equatorial) with increasing pressure.  
 796  
 797  
 798



799  
 800 **Extended Data Figure 10: Conceptual models of inner core growth scenarios.** Boundary  
 801 conditions (black arrows), resultant growth patterns (white arrows), and expected

802 topography (orange line, exaggerated for visualisation) for inner core models with (a)  
803 homogeneous growth rate, (b) equatorial heterogeneous growth rate<sup>11</sup>, (c) hemispherical  
804 heterogeneous growth rate<sup>15,16</sup>, and (d) equatorial and hemispherical heterogeneous growth  
805 rate, combining models b and c.  
806



807  
808 **Extended Data Figure 11:** Single crystal anisotropy of hcp Fe<sub>93.75</sub>Ni<sub>6.25</sub> alloy at 5500 K and  
809 360 GPa<sup>20</sup> with error range.  
810

# Figures

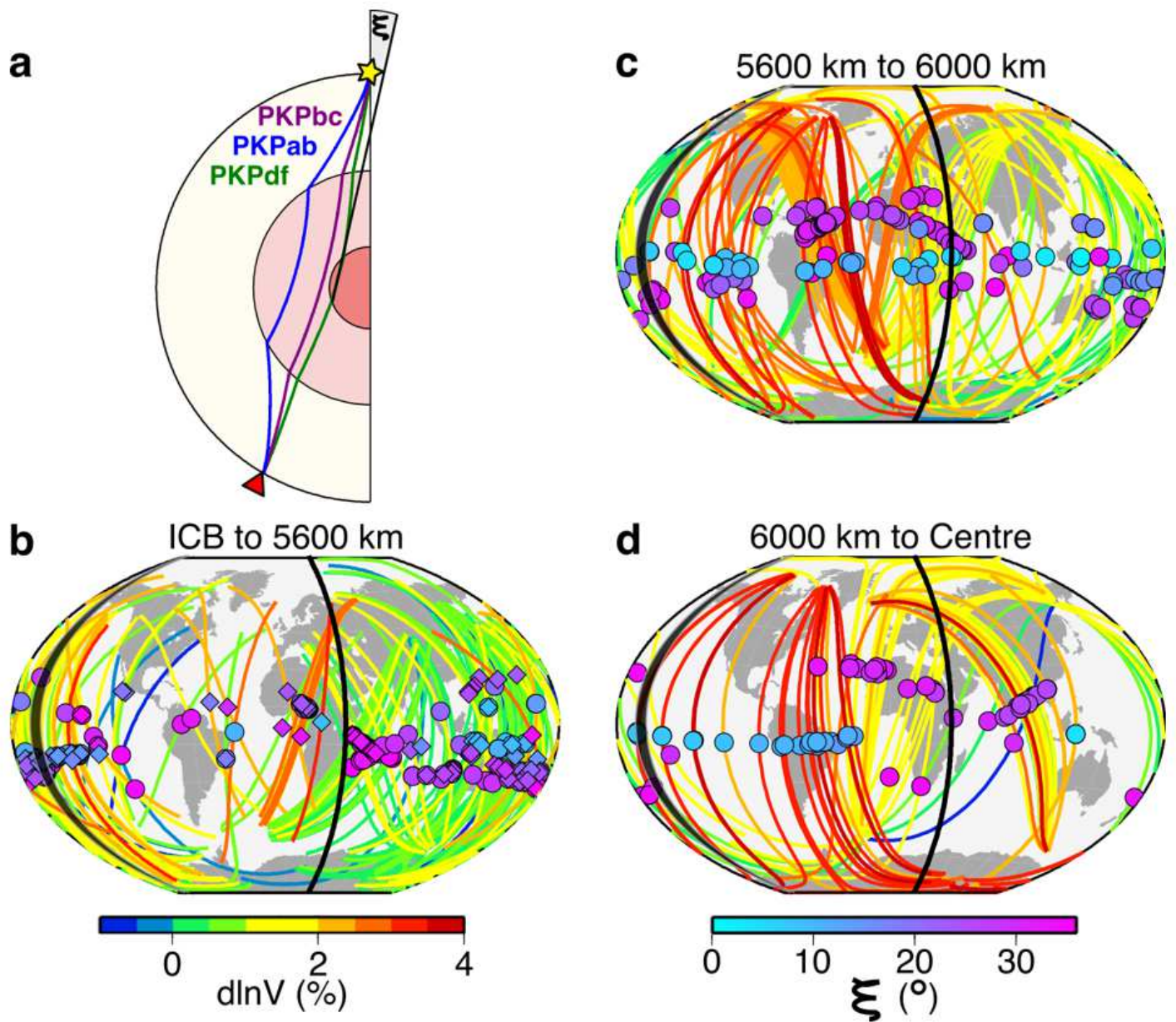


**Figure 1**

Sampling of the inner core with polar PKP rays. (a) Ray paths of PKP branches used in this study. PKPdf samples the inner core, while PKPbc and PKPab remain in the outer core.  $\xi$  is the angle that the PKPdf path in the IC makes with Earth's rotation axis. (b-d): Polar paths ( $\xi < 35^\circ$ ) from source to receiver colour-coded by effective velocity anomaly in the IC (line colour) and  $\xi$  (symbol colour) for paths turning between (b) 5200 and 5600 km depth, (c) 5600 km and 6000 km, and (d) 6000 km and Earth's centre. The total number of polar paths displayed is 530. The location of turning points for PKPdf rays are shown as diamonds (for PKPbc-df) and circles (for PKPab-df). Data shown exclude the South Sandwich Islands (SSI) to Alaska paths (see Methods and Extended Data Fig. 3). Equatorial paths are not displayed. Grey

region marks best-fitting WH boundaries determined in this study (see Methods) and solid line marks the EH boundary<sup>10</sup>.

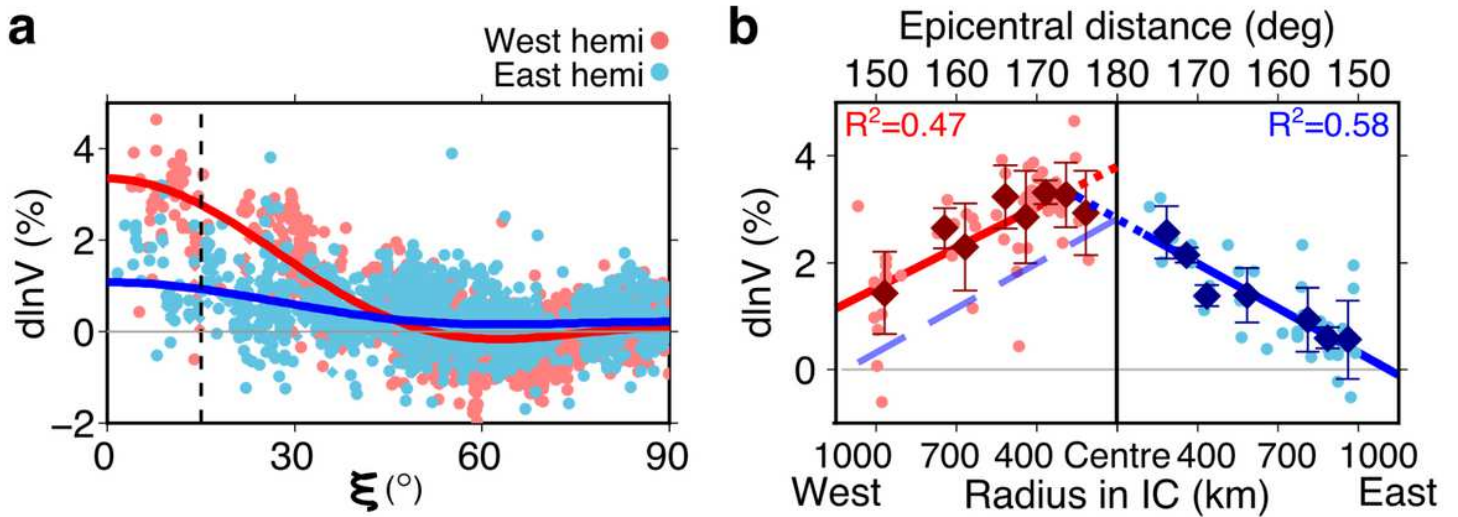


**Figure 2**

Effective velocity anomaly in the inner core from travel time observations as a function of  $\xi$  and epicentral distance. (a) Differential PKPab-df and PKPbc-df travel time anomalies as a function of  $\xi$ , expressed as effective velocity anomaly in the inner core, display a hemispherically distinct pattern implying stronger anisotropy in the WH (red) than in the EH (blue). Data from sources in the SSI to stations in Alaska are excluded (See Methods). (b) Effective IC velocity anomaly as a function of epicentral distance, and thus bottoming radius of the ray in the WH (left) and EH (right), for data with  $\xi \leq 15^\circ$  (those data that are left of the vertical broken line in (a)). Solid coloured lines indicate linear fits as a function of distance in the respective hemispheres with a mirror image across the centre of the Earth ( $180^\circ$ ) for the EH shown as a broken line. Moving averages (diamonds) and standard deviations at  $2.5^\circ$  increments in distance highlight the robustness of these trends. The extension of EH trend to meet the WH trend at  $\sim 175^\circ$  distance and 400 km radius is shown as a dotted blue line.

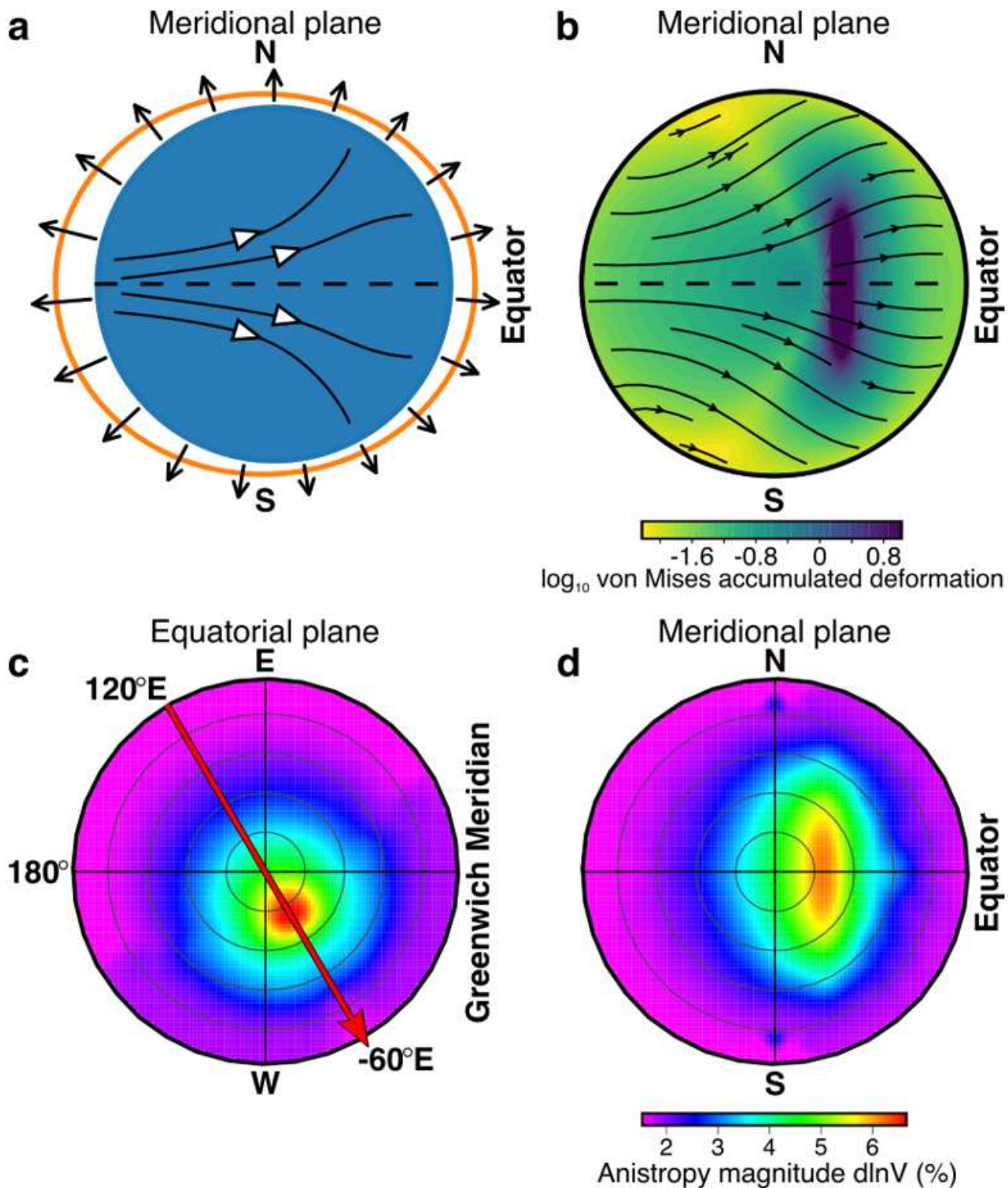


Figure 3

Inner core growth, strain and anisotropy. (a) Sketch combining preferential equatorial growth (driven by Taylor column convection in the outer core) and asymmetric growth rate, with imposed inner core growth rate at the boundary and internal flow shown by black and white arrows, respectively. (b) Asymmetric growth and movement in from the equator and towards the poles lead to lateral and vertical advection of the strongest deformation. Both (a) and (b) are drawn in the meridional plane along the axis of

translation with dashed line showing the equator. The strain field aligns hcp iron grains, producing strong anisotropy in the deep IC that is offset from the rotation (N-S) axis, as shown in (c) in the equatorial plane, and elongated parallel to the rotation axis, as shown in (d) the meridional plane along the direction of translation is shown by the red arrow in (c). Calculated with IC age of 0.5 Ga, S2 of 0.6, translation rate of 0.3, and translation direction from 120°E to -60°W.

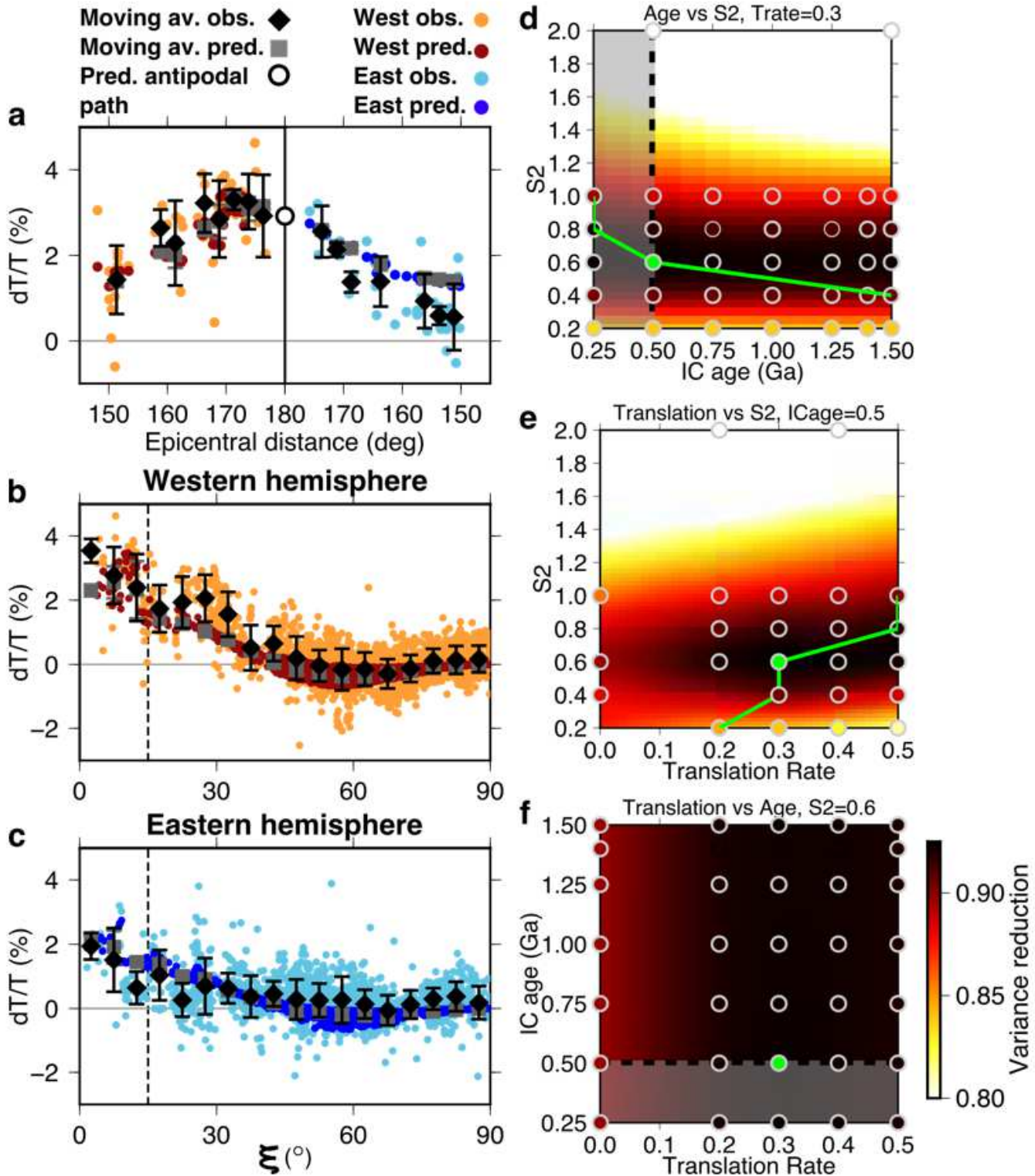


Figure 4

Predicted versus observed PKP velocity anomalies for hcp Fe<sub>93.75</sub>Ni<sub>6.25</sub> at 5500 K and 360 GPa<sup>20</sup> and trade-offs between IC age, S<sub>2</sub>, and translation rate. (a-c): Predicted (dark blue and red dots and with mean as grey squares) and observed (light blue and orange dots and with mean as black diamonds) effective velocity anomalies as a function of (a) epicentral distance for data with  $\xi \leq 15^\circ$ , marked by dashed line in (b) and (c), and as a function of  $\xi$  in the (b) western and (c) eastern hemispheres for an IC growth model with IC age=0.5 Ga, S<sub>2</sub>=0.6, translation rate=0.3, and translation direction from 120°E to -60°W. The open circle in (a) marks the predicted effective velocity anomaly for a path along the rotation axis. Error bars for the data show the mean and one standard deviation at 2.5° and 5° increments for panels (a), and (b) and (c), respectively. For calculation using pure hcp Fe see Extended Data Fig. 8. (d-f): Variance reduction of the model relative to the data illustrating the trade-offs between (d) IC age and S<sub>2</sub>, (e) S<sub>2</sub> and translation rate, and (f) translation rate and IC age. Grey circles mark tested values and the green point marks the best-fitting parameters, corresponding to the model in (a-c) and at which the 3D space is sampled. The green line tracks the best x-value at any given y-value. Models in the shaded region have IC ages that are likely too low based on core conductivity. Surface is interpolated with a “minimum curvature” spline.